Modelling wave group-scale hydrodynamics on orthogonal unstructured meshes

Reyns, Johan; McCall, Robert; Ranasinghe, Roshanka; van Dongeren, Ap; Roelvink, Dano

DOI
10.1016/j.envsoft.2023.105655

Publication date
2023

Document Version
Final published version

Published in
Environmental Modelling and Software

Citation (APA)
Reyns, J., McCall, R., Ranasinghe, R., van Dongeren, A., & Roelvink, D. (2023). Modelling wave group-scale hydrodynamics on orthogonal unstructured meshes. *Environmental Modelling and Software*, *162*, Article 105655. https://doi.org/10.1016/j.envsoft.2023.105655

Environmental Modelling and Software 162 (2023) 105655

Contents lists available at ScienceDirect

Environmental Modelling and Software

journal homepage: www.elsevier.com/locate/envsoft

Modelling wave group-scale hydrodynamics on orthogonal unstructured meshes

Johan Reyns [a,b,d,*], Robert McCall [b], Roshanka Ranasinghe [a,b,c], Ap van Dongeren [a,b], Dano Roelvink [a,b,d]

[a] Department of Coastal and Urban Risk & Resilience, IHE Delft Institute for Water Education, P.O. Box 3015, 2601 DA, Delft, The Netherlands
[b] Deltares, P.O. Box 177, 2600 MH, Delft, The Netherlands
[c] Department of Water Engineering and Management, University of Twente, P.O. Box 217, 7500 AE, Enschede, The Netherlands
[d] Faculty of Civil Engineering and Geosciences, Delft University of Technology, Stevinweg 1, 2628 CN, Delft, The Netherlands

ARTICLE INFO

Keywords:
Numerical modelling
Nearshore circulation
Infragravity waves
Unstructured meshes

ABSTRACT

An unstructured hydrodynamic model is presented that is able to simulate 2D nearshore hydrodynamics on the wave group scale. A non-stationary wave driver with directional spreading, with physics similar to XBeach (Roelvink et al., 2009) is linked to an improved and extended version of the existing unstructured flow solver Delft3D–FM (Kernkamp et al., 2011; Martyr-Koller et al., 2017). The model equations are discretised on meshes consisting of triangular and rectangular elements. The model allows for coverage of the model domain with locally optimised resolution to accurately resolve the dominant processes, yet with a smaller total number of grid cells. The model also allows a larger explicit time step, compared to structured models with similar functionality. The model reliably reproduces measured datasets of water levels, sea/swell and low frequency wave heights in laboratory and field conditions, and is as such widely deployable in a variety of simple and complex coastal settings to study nearshore hydrodynamics.

Software availability

The software framework of the model presented in this paper is Delft3D Flexible Mesh, under development since 2008 (Deltares, 2021). The source code is available free of charge from Deltares (https://oss.deltares.nl) after registration as a beta-test programme participant with software@deltares.nl. The framework is supported under Windows and CentOS7. The computational kernel is written in Fortran, and the complete compiled code distribution requires ~1Gb of disk space.

1. Introduction

Infragravity (IG) waves, defined as waves with periods of ~25–250 s, can represent a significant portion of the water level variance in the nearshore. These low frequency motions modulate several coastal processes, such as reef flat hydrodynamics (Péquignet et al., 2009; Pomeroy et al., 2012; Cheriton et al., 2020; Péquignet et al., 2014), rip current dynamics (MacMahan et al., 2004; Reniers et al., 2006, 2009), wave run up and overtopping (Cheriton et al., 2016; Billson et al., 2019), sediment resuspension and transport (de Bakker et al., 2016a; Rosenberger et al., 2020b), and dune erosion and barrier breaching (McCall et al., 2010; Baumann et al., 2017; Lashley et al., 2019; Anarde et al., 2020). Sources of wave energy in the IG frequency band are linked to the presence of wave groups. Theory (Longuet-Higgins and Stewart, 1962; Hasselmann, 1962) and observations (Kostense, 1985; Elgar et al., 1992; Herbers et al., 1994) show that in intermediate water depths pairwise non-linear difference interactions between sea–swell components in a wave group force a IG wave at the group frequency that is 180° out of phase with the wave group envelope. Upon propagating into shallow water depths, these IG waves shoal through resonant triad interactions (Janssen et al., 2003; de Bakker et al., 2015), transferring energy from the peak frequency toward IG frequencies at a rate dependent on the bed slope and the group frequency (Battjes et al., 2004; van Dongeren et al., 2007). Moreover, depth variations on the spatial scales of the wave groups cause a nett radiation stress gradient that forces free IG waves propagating both in onshore and offshore directions (Moura and Baldock, 2019; Contardo et al., 2021). In the outer surf zone, IG waves are generated by the time-varying breakpoint mechanism (Symonds et al., 1982; Contardo et al., 2018) on steep normalised bed slopes (Battjes et al., 2004). If normalised bed slopes are mild, and short waves and IG waves are in

---

[*] Corresponding author at: Department of Coastal and Urban Risk & Resilience, IHE Delft Institute for Water Education, P.O. Box 3015, 2601 DA, Delft, The Netherlands.

E-mail addresses: j.reyns@un-ihe.org (J. Reyns), robert.mccall@deltares.nl (R. McCall), r.ranasinghe@un-ihe.org (R. Ranasinghe), ap.vandongeren@deltares.nl (A. van Dongeren), d.roelvink@un-ihe.org (D. Roelvink).

https://doi.org/10.1016/j.envsoft.2023.105655
Received 27 December 2021; Received in revised form 2 February 2023; Accepted 7 February 2023

the shallow water regime, bound long waves are progressively released from the wave groups (Masselink, 1995; Baldock, 2012). When these conditions are not met, the bound wave degenerates with the breaking wave group, and IG generation is minimal (Baldock, 2012). In the inner surf zone, triad interactions between IG frequencies enhance IG wave non-linearity (Henderson et al., 2006; Thomson et al., 2006), and can cause IG wave breaking close to the shoreline (van Dongeren et al., 2007; de Bakker et al., 2016b). Similar triad interactions can transfer energy back to the short wave frequency band (Guedes et al., 2013; de Bakker et al., 2016b). Merging surf bore fronts can add additional energy to IG frequencies (Sénéchal N. Dupuis et al., 2001; Tissier et al., 2015). If the bed roughness in the surf zone is high, frictional dissipation is a significant IG energy sink (Péquignet et al., 2014; van Dongeren et al., 2013), Upon reflection off the coastline, IG waves radiate offshore as leaky waves, forming a cross-shore standing pattern (Guza and Thornton, 1985b), or they become refractively trapped as edge waves (Holman and Bowen, 1979; Herbers et al., 1995).

Given the important role of IG waves in coastal processes, substantial efforts were made over the last decades to model their generation, propagation and dissipation in various coastal settings. van Dongeren et al. (2003) provide a review of the analytical methods that have been explored to explain the generation of low-frequency wave energy. More recent (semi-)analytical studies include work on IG dynamics over variable topography to explore phase lags between the short wave forcing and the associated bound long wave (e.g. Zou 2011, Guérin et al. 2019, Zhang et al. 2020, Liao et al. 2021, Contardo et al. 2021, Liao et al. 2022), and on the generation of free long waves in the surf zone (Contardo et al., 2018). Nowadays, numerical models are the method of choice to explore IG variability on arbitrary profiles under dissipative conditions. List (1992), Van Leeuwen (1992) and Reniers et al. (2002) presented linearised models incorporating the IG generation mechanisms of Longuet-Higgins and Stewart (1962) and Symonds et al. (1982). Roelvink (1993b) and Karunarathna and Tanimoto (1995) presented 1D versions of a model solving the depth-integrated and short wave period-averaged non-linear conservation equations of mass and momentum on a finite difference grid. The wave forcing is provided by a wave group resolving wave model. Reniers et al. (2004) and van Dongeren et al. (2003) extended the approach to 2DH non-linear finite difference models for IG generation and propagation, again coupling a wave group resolving wave driver to a non-linear shallow water solver. This approach was ported to curvilinear grids by Roelvink et al. (2012), using a finite volume discretisation. Madsen and Sørensen (1997) used a Boussinesq-type model to simulate IG wave dynamics, resolving the short-wave motion as well as the long-wave motion. A similar model paradigm was used by, among others, Karunarathna et al. (2005), Cienfuegos et al. (2010), Nwogu and Demirbilek (2010) and Su et al. (2015). The last few years have seen an increase in popularity of non-hydrostatic models for the modelling of low-frequency wave dynamics. Models of this type were presented by Zijlema et al. (2011), Ma et al. (2012) and de Ridder et al. (2021). Detailed model hindcast studies of infragravity transformations in the surf zone of field sites and laboratory tests using the latter approach were reported by e.g. Rijnsdorp et al. (2015, 2021), de Bakker et al. (2016b), Fiedler et al. (2018), Lashley et al. (2018) and Risandi et al. (2020).

In the present paper, we adopt the approach of combining a 2DH non-linear shallow water equations solver with a wave group resolving wave driver. Most models of this class discretise the model equations on a structured, rectangular or orthogonal curvilinear grid (e.g. SHORECIRC, (Shi et al., 2003); Delft3D, (Reniers et al., 2004); XBeach, (Roelvink et al., 2009, 2012)). Although this type of grid schematisation provides relative flexibility in efficiently covering the model domain, an inherent drawback in the use of structured grids is that refinements (needed for output requirements, or for handling sharp spatial gradients in bathymetry or transport fields) necessarily extend far beyond the part of the domain where a finer resolution is needed. This can only be remedied in the structured grid approach by using nested models, or through domain decomposition. These latter approaches increase the computational cost of a model unnecessarily, and in the case where explicit numerical schemes are used, will also cause an unfavourable reduction of the maximum allowed timestep in deep areas, as the Courant–Friedrich–Lewy (CFL) condition (Courant et al., 1967) should be met to retain stable computational results. A second important drawback of structured curvilinear grids is the requirement of topological connection, which precludes for example the folding and reconnection of a curvilinear grid around islands or atolls, unless cyclic boundary conditions are implemented (Roelvink et al., 2013).

One approach to avoid these limitations is the use of unstructured grids, which are able to provide localised resolution changes, without affecting other parts of the grid. This flexibility allows for grid adaptations, where the grid resolution can now be optimised in function of the spatial scale of the locally dominant physical process to be modelled. One example of this would be a relative coarse offshore resolution sufficient to model the propagation of wave groups, combined with a finer resolution in regions where short wave dissipation, or long wave reflection is important. This geometrical flexibility has the added benefit that the grid resolution can also be optimised in function of the explicit time step restriction, as grid resolutions ideally are nowhere finer than they need to be to accurately discretise the flow phenomenon under consideration. Potential reduced accuracy because of the deviation of an unstructured grid from a uniform cartesian grid can be constrained by ensuring grid orthogonality and resolution smoothness, and by reducing the use of triangles as much as possible (Hirsch, 2007). Unstructured models has gained some popularity over the last decade to simulate mean (i.e. timescales longer than wave groups) nearshore circulation (e.g. Dietrich et al. (2012), Zheng et al. (2017), Wu et al. (2011)) and morphodynamics (e.g. Bertin et al. (2009), Guérin and Dodet (2016), Villaret et al. (2013)). However, to date there are no unstructured numerical models that can simulate nearshore hydrodynamics on the wave group scale. In this paper, we present such an unstructured wave model, and we test its ability to reproduce the wave measurements of a number of published datasets in field and laboratory settings.

In Section 2 we describe the formulations and the numerical approach that are used in the wave and flow modules of our model. Section 3 demonstrates the practical applicability of the model on a range of spatial and temporal scales. Section 4 contains discussion of the results and the conclusions.

2. Model formulations

The aim of the present model is to simulate the hydrodynamic circulation in the nearshore in response to instationary short-wave forcing on the time-scale of wave groups. The model should be able to simulate bound, free and refractively trapped long waves, and it should be able to handle run up and overwash. In our approach, we solve the depth-averaged, short-wave averaged non-linear shallow water equations on unstructured grids, that can be composed of a combination of triangular and rectangular cells. Short-wave effects are incorporated through radiation stress gradients which drive mean surf zone circulation, and low frequency motion on IG timescales. Moreover, short-wave induced Stokes drift varies on the wave group time and spatial scale. Lastly, bed shear stresses are enhanced by the presence of waves. As we do not solve for the individual short waves, we need a short wave driver, that is forced by directionally spread narrow-banded short wave spectra, and that solves the time-varying wave action balance in combination with a roller model over arbitrary 2D bathymetries.

2.1. Short wave module

2.1.1. Non-stationary wave model

In order to calculate the propagation and dissipation of organised wave energy in the nearshore, we largely follow Roelvink et al. (2009). The wave module solves the coupled non-stationary wave action (Eq. (1)) and roller energy balance (Eq. (8)) in geographical and directional space, taking into account dissipation by wave breaking and spatially varying bottom friction. We assume that the incident wave field is narrow-banded in frequency, so we can work with a single representative wave period, taken as $T_{m-1,0}$, and we neglect absolute frequency shifts in the wave action and roller balance.

$$\frac{\partial A}{\partial t} + \nabla \cdot \boldsymbol{c_g} A + \frac{\partial c_\theta A}{\partial \theta} = -\frac{D_w}{\sigma} - \frac{D_{bf}}{\sigma} \tag{1}$$

where A is the time-varying wave action density in geographical and directional space, defined as $A = \frac{E_w}{\sigma}$, $E_w = \frac{1}{8}\rho g H_{rms}^2$ is the wave energy density, t is time, ρ is the water density, θ the wave direction in the cartesian reference frame, D_w is the directionally distributed wave dissipation by breaking, D_{bf} is the directionally distributed wave energy dissipation by bottom friction, and ∇ represents the spatial gradient operator $\boldsymbol{i}\frac{\partial}{\partial x} + \boldsymbol{j}\frac{\partial}{\partial y}$, with $\boldsymbol{i}$ and $\boldsymbol{j}$ the unit vectors in x- and y-direction, respectively. Wind growth is not taken into account at present, although it can be an important energy source on the spatial scale ($\mathcal{O}(1\,\mathrm{km})$) at which this type of models is typically used (Drost et al., 2019).

The group velocity vector $\boldsymbol{c_g}$ with which the wave action propagates in geographical space is equal to

$$\boldsymbol{c_g} = \left(\frac{1}{2} + \frac{kh}{sinh(2kh)}\right)\frac{\sigma}{k} \cdot \frac{\boldsymbol{k}}{k} + \boldsymbol{u^L} \tag{2}$$

where $\boldsymbol{u^L}$ represents the depth-averaged flow velocity vector in the Lagrangian reference frame, h is the total water depth, and k the wave number magnitude. The refraction speed c_θ is given by

$$c_\theta = \frac{\sigma}{\sinh 2kh}\left(\frac{\partial h}{\partial n}\right) + \frac{\boldsymbol{k}}{k} \cdot \frac{\partial \boldsymbol{u}}{\partial n} \tag{3}$$

The derivative $\frac{\partial}{\partial n}$ indicates the gradient orthogonal to the local wave propagation direction θ. The wave number vector $\boldsymbol{k}$ is derived from the kinematics conservation equations (Massel, 1989):

$$\frac{\partial k_i}{\partial t} + c_{g,j}\frac{\partial k_i}{\partial x_j} + \frac{\partial \omega}{\partial x_i} = 0 \qquad i,j = 1,2 \tag{4}$$

where $\omega = \sigma + \boldsymbol{k} \cdot \boldsymbol{u}$, represents the absolute radial wave frequency. The intrinsic frequency σ is derived from the linear dispersion relation: $\sigma = \sqrt{gk \tanh kh}$.

Wave energy is dissipated through wave breaking and bottom friction. A number of wave breaking formulations is available (listed in Appendix A). By default, the formulation of Roelvink (1993a) is being used. The total, directionally integrated wave dissipation is then given by the product of the time-varying breaking dissipation and the fraction of breaking waves:

$$\begin{aligned} \overline{D}_w &= Q_b \alpha \frac{\sigma}{8\pi}\rho g \frac{H^3}{h} \\ Q_b &= 1 - \exp\left(-\left(\frac{H}{\gamma \frac{\tanh(kh)}{k}}\right)^n\right) \end{aligned} \tag{5}$$

where α is a free parameter of $O(1)$; ρ is the water density; g is gravitational acceleration; γ is the breaker parameter, H is the wave height varying on the timescale of wave groups, and n is a shape factor for the wave breaking probability distribution. $\gamma\frac{\tanh(kh)}{k}$ represents a measure for the maximum expected wave height for the local water depth h. The breaker dissipation is distributed among the directional bins according to the directional distribution of the wave energy.

We express the time-averaged, directionally integrated bottom frictional dissipation of wave energy as $\overline{D}_{bf} = \langle|\boldsymbol{\tau_b} \cdot \boldsymbol{u_{rms}}|\rangle = \frac{1}{2}\rho f_w \langle|\boldsymbol{u_{rms}}|^3\rangle$, where the root mean square orbital velocity magnitude $|\boldsymbol{u_{rms}}|$ is approximated from the linear wave theory expression for the orbital velocity (Eq. (6)), and f_w is a parameter of $\mathcal{O}(0.01)$–$\mathcal{O}(0.1)$, depending on the bottom characteristics (Booij et al., 1999; van Dongeren et al., 2013).

$$|\boldsymbol{u_{rms}}| \approx \frac{H_{rms}\omega}{2\sqrt{2}\sinh(kh)} \tag{6}$$

Considering the slowly varying dissipation in wave groups, we can time-average D_{bf} over the representative wave period. Therefore, we can use the monochromatic approximation for the time-average of the third even velocity moment $\langle|\boldsymbol{u_{rms}}|^3\rangle$ (Eq. (7)) to calculate $\overline{D}_{bf}$ (Guza and Thornton, 1985a):

$$\langle|\boldsymbol{u_{rms}}|^3\rangle = 1.20\langle|\boldsymbol{u_{rms}}|^2\rangle^{3/2} = 0.42|\boldsymbol{u_{orb}}|^3, \text{ with } |\boldsymbol{u_{orb}}| \approx \sqrt{2}|\boldsymbol{u_{rms}}| \tag{7}$$

The resulting bottom dissipation $\overline{D}_{bf}$ is distributed among the directional bins in a manner analogous to the redistribution of the dissipation resulting from wave breaking processes.

The lack of a wind source term limits the applicability of the model to domains and applications where local wind growth is of secondary importance.

2.1.2. Roller model

In order to account for the observed spatial lag between the start of depth-induced breaking and the development of wave setup and wave-related circulation (Bowen et al., 1968; Nadaoka and Kondoh, 1982), the roller model concept (Roelvink and Stive, 1989; Nairn et al., 1991) is used. The breaking wave dissipation D_w acts as the source term for the roller energy. The roller propagates through the surf zone with wave celerity c, and following the carrier wave idea, where local wave and roller directions are assumed to be equal, allows us to reuse the refraction velocity c_θ used in the wave action balance (Eq. (1)):

$$\frac{\partial E_r}{\partial t} + \nabla \cdot \boldsymbol{c} E_r + \frac{\partial c_\theta E_r}{\partial \theta} = D_w - D_r \tag{8}$$

where E_r is the roller energy, $\boldsymbol{c}$ is the wave celerity vector equal to $\frac{\sigma}{\boldsymbol{k}}$, and D_r is the directionally distributed roller energy dissipation, the magnitude of which is calculated as (Reniers et al., 2004):

$$D_r = \frac{2\,g\beta_r E_r}{c} \tag{9}$$

in which β_r is a parameter of $\mathcal{O}(0.1)$, representing the slope of the internal boundary between the roller and the underlying 'wave motions'. The resulting wave and roller fields feed into the radiation stress tensor components, calculated using linear wave theory (Reniers et al., 2002):

$$S_{xx} = \int \left[\left(\frac{c_g}{c}\ (1 + cos^2\theta) - \frac{1}{2}\right)\ E_w + cos^2\theta\ E_r\right] d\theta \tag{10a}$$

$$S_{xy} = \int \left[\frac{c_g}{c}\ cos\theta\ sin\theta\ E_w + cos\theta\ sin\theta\ E_r\right] d\theta \tag{10b}$$

$$S_{yy} = \int \left[\left(\frac{c_g}{c}\ (1 + sin^2\theta) - \frac{1}{2}\right)\ E_w + sin^2\theta\ E_r\right] d\theta \tag{10c}$$

The wave-related forcing terms in the depth-averaged flow momentum equations (Eq. (22)) are then expressed in terms of the radiation stress gradients:

$$F_{w,x} = -\left(\frac{\partial S_{xx}}{\partial x} + \frac{\partial S_{xy}}{\partial y}\right) \tag{11a}$$

$$F_{w,y} = -\left(\frac{\partial S_{xy}}{\partial x} + \frac{\partial S_{yy}}{\partial y}\right) \tag{11b}$$

2.1.3. Numerical implementation

Eq. (1) and (8) are discretised in geographical space on a staggered orthogonal, smooth unstructured grid consisting of combinations of triangles and rectangles. A user-defined number of bins defines the directional grid. Spatial advection terms are determined from an explicit higher order discretisation scheme, combined with a monotonized central flux limiter for non-equidistant grids (Hou et al., 2012) to limit numerical diffusion and to ensure total variation diminishing (TVD) properties of the scheme (Deltares, 2021). All wave properties are determined in the cell centres. Collecting the dissipation terms in one variable D, Eq. (1), written in terms of wave energy, is discretised as follows:

$$\frac{ee^{n+1}_{k,i\theta} - ee^{n}_{k,i\theta}}{\Delta t} + \text{Adv}_{k,i\theta} + \text{Ref}_{k,i\theta} + \frac{D^*_k}{E^*_k} ee^*_{k,i\theta} = 0 \tag{12}$$

where k is the cell number, $i\theta$ the directional bin, n represents the time level, $*$ indicates the values after the advection and refraction step, ee is the wave energy in cell k and directional bin $i\theta$, E is the directionally integrated wave energy. Terms $\text{Adv}_{k,i\theta}$ for the spatial advection and $\text{Ref}_{k,i\theta}$ for the wave refraction are elaborated on next.

Using Gauss' theorem, the cell-centre based advection discretisation $\text{Adv}_{k,i\theta}$ in Eq. (12) is equal to the sum of the face-based advection contributions $\text{w}_L\text{Adv}_{L,i\theta}$, and divided by the cell area A_k (Eq. (13)).

$$\text{Adv}_{k,i\theta} = \frac{1}{A_k} \sum_{L \in \Gamma} \text{w}_L \text{Adv}_{L,i\theta} \tag{13}$$

where L indicates the face under consideration, w_L is the face width of L, and Γ is the cell boundary of cell k. Face based advection flux $\text{Adv}_{L,i\theta}$ is the sum of a first order upwind contribution $\text{Adv}_{L,upw}$ (Eq. (14)) and a higher order, flux-limited correction term $\text{Adv}_{L,ho}$ (Eq. (16a)). The first order upwind contribution is equal to:

$$\text{Adv}_{L,upw} = \begin{cases} C_{g\,L,i\theta}\text{ee}_{B,i\theta}, & C_{g\,L,i\theta} > 0 \\ C_{g\,L,i\theta}\text{ee}_{A,i\theta}, & C_{g\,L,i\theta} < 0 \\ 0, & C_{g\,L,i\theta} = 0 \end{cases} \tag{14}$$

where $C_{g\,L,i\theta}$ is the cell volume weighted wave group velocity in the face-normal direction for directional bin $i\theta$, calculated from the values in A and B. In order to explain the construction of the higher order correction term $\text{Adv}_{L,ho}$, we assume a wave energy flux from cell B to cell A in the following (Fig. 1). An equivalent reasoning holds for a flux from cell A to cell B. The construction of the higher order correction term for the face-based advection flux $\text{Adv}_{L,i\theta}$ happens on a line through the cell circumcentres of cells A and B, based on the wave energy in the cells adjacent to cell B. These cells are called B_{upw1} and B_{upw2} in Fig. 1. We aim at constructing the correction at the location of the crossing $B_{c,upw}$ between lines A–B and B_{upw1}–B_{upw2}. Note that if either one of these cells does not exist, the intersection collapses to the cell centre of B_{upw1}, and the approach will reduce to a classical second-order upwind correction, such as for curvilinear discretisations. Thus, the stencil applied here consists of cells A, B, B_{upw1} and B_{upw2}. Based on the values of the wave energy in the latter two cells, a value $\text{Adv}_{B,sl}$ is determined at location $B_{c,upw}$:

$$\text{ee}_{B,sl,i\theta} = \text{sl}_{B_{upw1}}\text{ee}_{B_{upw1},i\theta} + \text{sl}_{B_{upw2}}\text{ee}_{B_{upw2},i\theta} \tag{15a}$$

$$\text{sl}_{B_{upw1}} = \frac{dB1}{dB1 + dB2} \tag{15b}$$

$$\text{sl}_{B_{upw2}} = \frac{dB2}{dB1 + dB2} \tag{15c}$$

$$\gamma_{B,sl} = \frac{\text{dx}}{\text{d}_{\text{upw}}} \tag{15d}$$

The higher-order correction flux $\text{Adv}_{L,ho}$ is then:

$$\text{Adv}_{L,ho} = \alpha_A \max(1 - \frac{\Delta t |C_{g\,L,i\theta}|}{dx}, 0)\Psi(r)(C_{g\,A,i\theta} - C_{g\,B,i\theta}) \tag{16a}$$

$$r = \frac{\text{ee}_{A,i\theta} - \text{ee}_{B,i\theta}}{\text{ee}_{B,i\theta} - \text{ee}_{B,sl,i\theta}} \tag{16b}$$

$$\Psi(r) = \max(\min(\min(\frac{r}{\alpha_A}, \frac{1+r}{2}), \frac{1}{\alpha_A}), 0) \tag{16c}$$

where r is the ratio of the wave energy slopes along line A–$B_{c,upw}$, α_A is the fraction represented by cell A in the volume weighting, and $\Psi(r)$

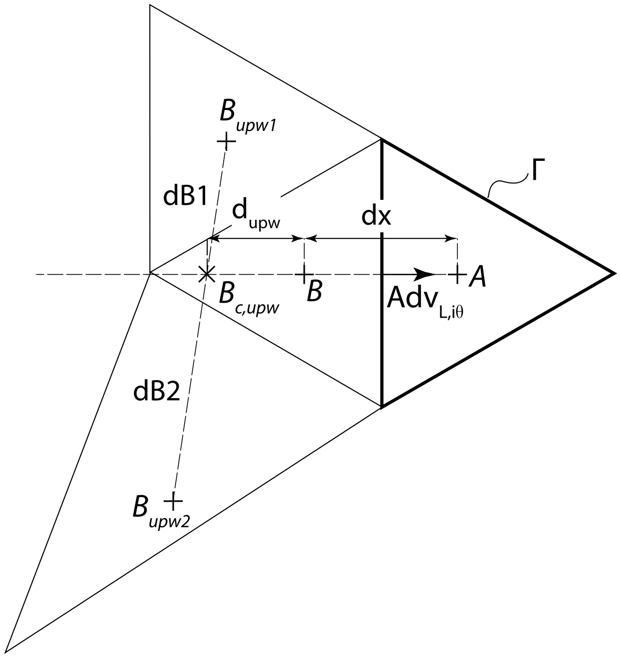

Fig. 1. Stencil to calculate higher order spatial advection contribution $Adv_{L,i\theta}$.

represents the Monotonized Central (MC) difference limiter suppressing wiggles resulting from higher order advection (Hou et al., 2012). The roller energy balance (Eq. (8)) is discretised in a similar fashion.

The refraction term $\text{Ref}_{k,i\theta}$ is discretised in directional space with a second order upwind approach as follows:

$$\text{Ref}_{k,i\theta} = \frac{\left(\text{Ref lux}_{k,i\theta} - \text{Ref lux}_{k,i\theta-1}\right)}{\Delta\theta} \tag{17}$$

$$\text{Ref lux}_{k,i\theta} = \begin{cases} C_{\theta\,L,i\theta}\left(1.5\text{ee}_{k,i\theta} - 0.5\text{ee}_{k,i\theta-1}\right), & C_{\theta\,L,i\theta} > 0 \\ C_{\theta\,L,i\theta}\left(1.5\text{ee}_{k,i\theta+1} - 0.5\text{ee}_{k,i\theta+2}\right), & C_{\theta\,L,i\theta} < 0 \\ 0, & C_{\theta\,L,i\theta} = 0 \end{cases} \tag{18}$$

where $\text{Ref lux}_{k,i\theta}$ is the wave energy flux by refraction on the interface between directional bin $i\theta$ and $i\theta+1$, and $C_{\theta\,L,i\theta}$ is the average refraction velocity on the same interface, calculated based on Eq. (3).

Eqs. (1) and (8) are solved with explicit forward Euler timestepping. The maximum allowed timestep Δt is determined from

$$\Delta t = \text{CFL} \min_{ncells} \left. \frac{A_k}{\sum_{i\theta \in n\theta} \sum_{L \in \Gamma} \text{w}_L C_{g\,L,i\theta}} \right|_{C_{g\,L,i\theta} > 0} \tag{19}$$

2.1.4. Stationary wave model

In addition to the non-stationary wave model described in the previous section, an additional wave driver is included in the code to provide the stationary wave fields used in the single direction approach of Roelvink et al. (2018). In this approach, the stationary wave driver updates the wave field in full directional space, and determines the mean wave direction in every flow node. The wave groups in the non-stationary model are subsequently advected along this mean direction only, preserving the groupiness much better, and yielding more reliable estimates of the infragravity wave heights.

For our present purpose, the module solves the wave energy balance using an implicit first order upwind scheme with pseudo timestepping and quadrant sweeping to ensure convergence of the solution. An outline of the implementation is given in Appendix C.

2.2. Momentum and continuity equations for unsteady flow

The short-wave averaged, wave group resolving, depth-averaged unsteady flow patterns are described using the non-linear shallow water equations in the Generalised Lagrangian Mean framework (Andrews and McIntyre, 1978; Nguyen et al., 2021). The model equations are solved for the Lagrangian velocities $\boldsymbol{u^L}$. These wave period-averaged water particle velocities, are defined as the sum of the Eulerian velocities $\boldsymbol{u^E}$, the velocity field observed from a fixed point at the bed, and the Stokes drift $\boldsymbol{u^S}$, calculated from linear wave theory.

$$\boldsymbol{u^L} = \boldsymbol{u^E} + \boldsymbol{u^S} \tag{20a}$$

$$\boldsymbol{u^S} = \frac{\left(E_w + 2\ E_r\right)}{\rho h c} \cdot \frac{\boldsymbol{k}}{k} \tag{20b}$$

where the wave energy E_w, the roller energy E_r and the wave number vector $\boldsymbol{k}$ are obtained from the wave module.

We express conservation of mass as

$$\frac{\partial \zeta}{\partial t} + \nabla \cdot \left(h\ \boldsymbol{u^L}\right) = 0 \tag{21}$$

in which ζ is the water level. Conservation of momentum is expressed as

$$\frac{\partial \boldsymbol{u^L}}{\partial t} + \nabla \cdot \left(\boldsymbol{u^L u^L}\right) + \boldsymbol{f} \times \boldsymbol{u^L} = -g\nabla\zeta + \nabla \cdot \nu \left(\nabla \boldsymbol{u^L} + (\nabla \boldsymbol{u^L})^T\right) + \frac{\boldsymbol{\tau_w}}{\rho h} - \frac{\boldsymbol{\tau_b}}{\rho h} + \frac{\boldsymbol{F_w}}{\rho h} \tag{22}$$

where the first term in the left hand side represents inertia, the second term advection, and the third earth rotational effects. The first term in the right hand side of the equation represents the pressure gradient, the second term horizontal turbulent mixing, the third and fourth term the influence of wind and bottom roughness, respectively, and the fifth term forcing by waves as calculated by Eq. (11). $\boldsymbol{f}$ is the Coriolis vector, ν is breaker-induced turbulent eddy viscosity equal to $h\left(D_r/\rho\right)^{\frac{1}{3}}$ (Battjes, 1975). Wind shear stress $\boldsymbol{\tau_w}$ is determined by

$$\boldsymbol{\tau_w} = \rho C d_a |\boldsymbol{u_{10}}| \boldsymbol{u_{10}} \tag{23}$$

with Cd_a a wind friction parameter, and $\boldsymbol{u_{10}}$ the wind velocity vector. The bed shear stress $\boldsymbol{\tau_b}$ is calculated following the parametrisations of Soulsby (1997) or Ruessink et al. (2001), and by using the Eulerian velocity definitions $\boldsymbol{u^E}$ in the bottom stress formulation.

The shallow water equations are discretised with a finite volume approach on an orthogonal Arakawa–B grid, resulting in a set of facenormal velocities and cell centre water levels. The momentum equations are solved conservatively using the approach of Perot (2000). The cartesian advection and diffusion vector components are reconstructed in the cell centres, and interpolated back to the cell faces, after which they are rotated in face-normal direction. The advection contribution is discretised using an higher-order limited upwind scheme, using a similar method as described in Section 2.1.3. Time integration is done semi-implicitly with a predictor–corrector scheme. First, the face-normal velocities are calculated explicitly. This velocity field is then substituted in the continuity equation to obtain the water levels at the new time level using the θ–method. The updated velocities are then obtained from back-substitution using the new water levels in the pressure gradient term. Full details of the methodology can be found in Kernkamp et al. (2011),Martyr-Koller et al. (2017) and Deltares (2021). The explicit time discretisation to solve the momentum equation leads to a time step restriction where the flow time step is minimised based on the requirement that the ratio between the water volume in a cell and the outgoing discharges be positive within a time step. As water levels are solved for implicitly, the long wave celerity should not be included in the restriction (Deltares, 2021). The global model time step is then the minimum of the flow and the wave time step derived from Eq. (19).

Drying and flooding is taken into account in the spatial discretisation by setting face-normal velocities, the advection contribution, external force terms and the viscous fluxes to zero when the depth on a cell face is smaller than a threshold value. In the temporal discretisation, the drying–flooding check is performed at the beginning of the time step, and a second time after the water level equation is solved. If the updated water levels are lower than the local bed level, the cell is removed from the system of equations, and the time step is repeated (Deltares, 2021).

2.3. Boundary conditions

The wave model is forced by spatially varying wave energy time series that are modulated on the timescale of wave groups following the procedure of van Dongeren et al. (2003). A single-summation, random phase approach is used whereby at every offshore wave boundary point, the sea–swell water level signal is derived from the input spectrum for a finite number of discrete frequency components and directions using linear wave theory, according to the directional distribution of the spectrum. These wave components are integrated over directional space, and the absolute value of the Hilbert transform of this signal yields the water level envelope. This water level envelope is distributed back in directional space according to the directional variance distribution, and converted to wave energy. The bound long waves associated with the sea–swell wave groups are derived from frequency-difference interactions between the swell components using the equilibrium theory of Hasselmann (1962) and Okihiro et al. (1992). Lateral open boundaries that have no explicit wave signal imposed are of the Neumann type, causing some disturbances under obliquely incident waves. The influence of these disturbances can be mitigated with an appropriate choice of boundary locations.

On the open flow boundaries an absorbing–generating boundary condition is imposed (van Dongeren and Svendsen, 1997), that combines the slowly varying tide-surge water level with the discharges associated with the bound long waves generated by the wave model. The boundary absorbs perpendicularly and obliquely outgoing free waves by locally reconstructing the outgoing characteristics and subtracting them from the incoming signal. Lateral flow boundaries use the approach of Roelvink and Walstra (2004), avoiding spurious circulations by combining the specification of longshore water level gradients with switching off cross-boundary velocity gradients. Cross-shore velocity gradients along the boundary are unaffected. Combined with an offshore water level boundary, this yields a well-posed system of equations to be solved.

2.4. Model applicability

This combination of a non-linear circulation model with a linear phase-averaged wave driver allows for the propagation of wave groups with their associated bound long waves from offshore to the nearshore. Short wave refraction and dissipation force wave group scale water motions, that can non-linearly interact and dissipate on IG frequency scales. As we model short waves on the time scale of wave groups, and not the individual waves, non-linear energy transfers between sea–swell and IG frequency bands are not accounted for in the short wave energy balance. Neither can we reproduce processes like short wave bore merging, which add to the IG energy content in the inner surf zone (van Dongeren et al., 2007; Tissier et al., 2015). In the present approach, IG waves do however influence the short wave energy propagation and dissipation, by modulating the local depths in shallow water, where IG wave heights can be of the same order of magnitude as the short waves (Pomeroy et al., 2012; Péquignet et al., 2014).

3. Model verification

The correctness of the implementation and some of the model's key features are demonstrated in the present section using a number of case studies. The theoretical Zelt case (Zelt, 1986; Özkan-Haller and Kirby, 1997) is used to check long wave propagation, flooding and drying, and the performance of the 2D absorbing–generating boundary. The Boers flume study (Boers, 1996) demonstrates short and long wave

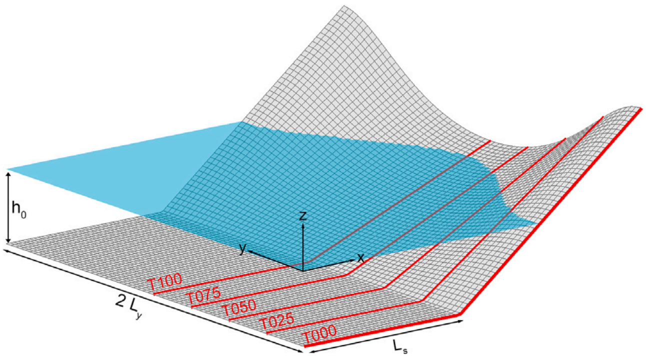

Fig. 2. Problem geometry Zelt test case. L_y is the half wavelength of the sinusoidal bay; L_s is the width of the shelf; Txxx indicates the number of the line where the run-up heights are recorded in Fig. 3(**a**).

transformation over a barred profile. Extending to 2DH cases, the COAST3D test case (Soulsby, 2001) demonstrates the capabilities of the model in reproducing non-stationary wave fields in realistic field settings. The DELILAH field testcase (Birkemeier et al., 1997) is used to demonstrate the computational advantages of the stationary refraction approach (Roelvink et al., 2018) in combination with unstructured grids. The PILOT field case (Clark et al., 2020) applies the model to reproduce the hydrodynamics of a fringing reef on the island of Guam, demonstrating how local grid refinements allow an efficient computation of wave properties in a topographically complex setting. This is taken one step further in the final field case, which simulates the refraction of a swell field around Buck Island Reef National Monument, a Caribbean island sheltered from incident waves by a reef complex (Rosenberger et al., 2020a).

3.1. Zelt solitary wave run-up

Any process-based surf zone model has to deal with the numerical treatment of a moving shoreline. In the present model, the shallow water equations are solved on a stationary mesh, and the shoreline is defined as the interface of a wet and a dry flow cell. Whether a cell face is a shoreline is determined from the neighbouring water levels using an upwind reconstruction (Deltares, 2021). The land/water interface is moved in discrete steps with an accuracy constrained by the local grid size.

In order to test the accuracy of the wetting/drying implementation for different grid configurations, and to check the performance of the absorbing offshore boundary, we replicate the tsunami run-up model devised by Zelt (1986). This testcase simulates the shoreward propagation of a tsunami, modelled as a non-linear solitary wave, over a flat shelf with depth h_0 and width L_s into a sinusoidal shaped bay with steep side promontories. The tsunami refracts and reflects off the coast, and propagates out of the domain. The beach slope in the centre of the bay is 1/10, and the promontories have a maximum slope of 1/5. The wave length of the bay is $2L_y$. The characteristic water depth h_0 was chosen by Zelt (1986) as $0.4L_y/\pi$. If we locate the origin of the coordinate system on the SW corner of the domain, with x increasing toward the coast (Fig. 2), the bottom z_b is defined by

$$z_b = \begin{cases} -h_0 & \text{if } x \leq L_s \\ -h_0 + \frac{0.4\ (x-L_s)}{3-\cos(\pi\ y/L_y)} & \text{if } x > L_s \end{cases} \tag{24}$$

At the offshore boundary, we define the time-varying water level ζ_{in} as

$$\zeta_{in}(t) = \alpha\ h_0\ sech^2\left(\sqrt{\frac{3\ g}{4\ h_0}\alpha(1+\alpha)}(t-t_0)\right) \tag{25}$$

where α is the non-linearity parameter defined as H/h_0, H is the characteristic wave height of the tsunami in deep water, g is gravitational acceleration, and t_0 is a phase shift such that the incoming signal at t=0 is equal to $0.1H$ (Roelvink et al., 2009). As we compare our results to Özkan-Haller and Kirby (1997), α is set to their value of 0.02. This value was chosen to ensure sufficiently high run-up, as the characteristic length of the solitary wave, and hence the slope it ‘feels’, scales with $1/\sqrt{\alpha}$ (Zelt, 1986).

The model was set up to solve the non-linear shallow water equations using three grid versions: (1) a rectangular grid with a square net cells with a resolution of 0.125 m, aligned with the x-axis; (2) a rectangular grid with the same resolution, rotated counter-clockwise by 30°, to show the robustness of the solution in a framework not aligned with the coordinate axes; (3) an orthogonal triangular grid with a resolution of 0.08 m, to minimise shoreline staircase effects. The half-bay width L_y was set to 8 m, resulting in $h_0 = 1.019$ m, and $L_s = L_y$. The bathymetry was then constructed using Eq. (24), and imposed in the flow nodes of the model grid. The absorbing–generating boundary was forced with Eq. (25), taking the first 33.5 s to send the tsunami into the domain. After that, only reflected signals pass the offshore boundary. Both lateral boundaries have a no-flux condition, and thus act as a sidewall. The model was run without friction and viscosity, following Zelt (1986) and Özkan-Haller and Kirby (1997). Maximum run-up time series were recorded using numerical run-up gauges on the unstructured grid. To that end, 5 polylines were added to the model (Fig. 2), and at the start of the run, an administration of crossed flow links was created per polyline. The waterlevel value along each line for a model time step was then determined as the topographically highest flow link joining a wet and a dry flow node in each polyline’s link administration.

As stated before, the outcomes of runs (1)–(3) were compared with the model results of Özkan-Haller and Kirby (1997) (Fig. 3). Özkan-Haller and Kirby (1997) used a collocated spectral method where solutions to the shallow water equations are determined on a temporally and spatially adaptive grid using global, directionally decoupled polynomial approximations. This resulted in a very high resolution in the cross-shore direction in a natural way, thus getting very accurate estimates for momentary coastlines at every time step. Fig. 3(a) shows the vertical run-up normalised with the characteristic wave height H in function of normalised time $t\ \sqrt{g\,h_0}/L_y$. Runs (1)–(3) all show similar behaviour, demonstrating the effectiveness of the absorbing boundary under different grid configurations. The run with the rotated grid (run (2)) has a slight negative phase shift as compared to the run with the ‘aligned’ rectangular grid, showing a better comparison with Özkan-Haller and Kirby (1997). Similarly to the structured models of Roelvink et al. (2009) and Hubbard and Dodd (2002), the unstructured model is only moderately capable of reproducing the secondary peak in the centre of the bay (at t/T=4 for profile T100), attributed by Zelt (1986) to wave focusing of the headland reflections. Roelvink et al. (2009) cites a staircase shoreline, a lack of resolution and grid line-oriented spatial derivatives as potential culprits for this diminished performance. To test this hypothesis, run (3) was included in our analysis. The triangular grid has a finer resolution than the rectangular versions, and moreover, it has no strict directionality along grid lines in the solution process. The time series corresponding to this run (green line in Fig. 3(a)) show a better phasing of the vertical wave run-up with the results of Özkan-Haller and Kirby (1997), as compared to the runs with rectangular grids. This result hints at the interplay between local bed slope and the grid resolution as the main reason for the observed discrepancies. The amplitude of the secondary water level peak is however still too small (∼ 10% difference). In order to assess the grid resolution effect in more detail, we performed a grid convergence test following Celik et al. (2008). Therefore, three additional runs were made with uniform resolutions of 0.04, 0.08 and 0.16 m, and the maximum run up value was used to evaluate the performance of the runs. The apparent order of grid convergence is 1.1, showing that the discretisation method to

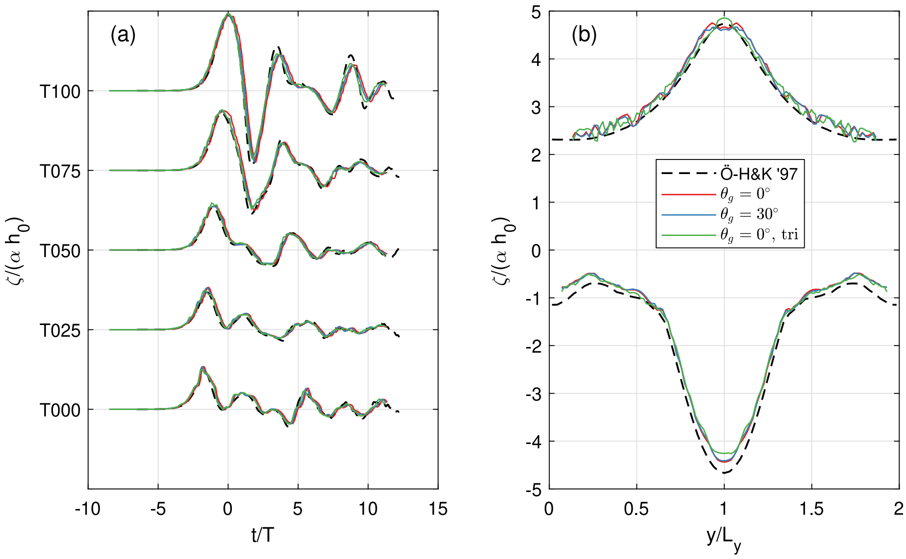

Fig. 3. Zelt tsunami run-up. (**a**) run-up time series at equally spaced alongshore transects; (**b**) Maximum run-up and rundown. Dashed line: results from Özkan-Haller and Kirby (1997). Red line: no grid rotation; blue line: grid rotated over 30°; green line: triangular grid. T is the time normalisation factor $L_y/\sqrt{g\,h_0}$. Note that the time series origin is shifted to the time of maximum wave height in $y/L_y = 1$.

determine the shoreline position is slightly more accurate than first order. The numerical uncertainty of the maximum run up for the finest grid is about 8 %.

The time series of points located away from the bay centre line show good correspondence with Özkan-Haller and Kirby (1997), with run (3) slightly outperforming both runs with rectangular grids (Table B.3).

Fig. 3(b) shows the maximum and minimum normalised vertical run-up $\zeta/\alpha\,h_0$ in function of the normalised longshore position y/L_y. All three runs overpredict the run-up by about 2%, and the error slightly increases toward the edges of the domain. All maximum shorelines show a serrated pattern away from the bay centre, resulting from staircasing on the relatively steeper slope. Run (3) reproduces the maximum shoreline position in the central part of the bay the best, although its maximum is higher than that of the reference data. All runs slightly underpredict the maximum run-down by ~5%, with run (3) performing the worst. The staircasing effect is less pronounced for the run-down, as the bed level gradients are smaller in the deeper areas of the model. Overall, based on the error metrics, the reproduction of the run-up/run-down patterns is judged satisfactory for all three model configurations (Table B.3), and comparable to results from similar modelling approaches (Hubbard and Dodd, 2002; Roelvink et al., 2009). It should be noted that the present case study simulates run-up using the non-linear flow solver only. When combining the flow and the wave solver in a model setup, the run-up part related to the short waves cannot be modelled, as we only resolve the wave group, and not the individual waves.

3.2. Boers flume study

The performance of the model in generating suitable wave boundary conditions, and in simulating wave-driven flow over a barred profile is tested by comparing the numerical results with data measured by Boers (1996). Although the case does not leverage the specific benefits of using unstructured grids, it demonstrates the correct implementation of the model equations. Boers (1996) reproduced the conditions of the LIP11D tests reported in Sánchez-Arcilla A. Roelvink et al. (1994) on a fixed bed in the Large Wave Flume at Delft University of Technology. The test conditions were Froude-scaled with a factor of 5.6 relative to the LIP11D experiment. The wave flume is 40 m long and 0.8 m wide, and has a maximum depth of 1.05 m. The wave-generating paddle board is of the hydraulically-driven piston type, with second-order steering and active reflection compensation to remove free reflected waves from the flume during the run. The model bed was constructed from sand, topped by a concrete layer to smoothen the surface, and mimicked a nearshore profile with a single bar and a surf zone trough (Fig. 4). The spatial axis of the measurements has its origin at the toe of the profile slope, 4.5 m from the wave generator. Boundary time series were constructed by repeating a short cycle with a length of ~75 times T_p and applying a f_p dependent high-pass filter to compensate for paddle board artefacts. By repeated experiments using the same boundary conditions, detailed hydrodynamic measurements were made at 70 locations throughout the flume at 20 Hz. The experimental parameters represent different wave steepnesses, related to the original goal of the LIP11D tests to measure during erosive and accretive conditions. During tests 1 A and 1B, waves were breaking throughout the flume. During test 1C, the incident short waves shoaled before breaking on the bar. During tests 1B and 1C, low frequency (LF) energy increased steadily toward the shoreline. Test 1 A shows shoaling of the low-frequency waves just before the bar, and a decrease of their amplitude in the trough. The measured values for H_s and T_p at the toe of the profile, and the cycle duration per condition, are listed in Table 1.

Table 1
Experimental conditions of the Boers (1996) flume study.

Experiment	H_{sig} [m]	T_{p} [s]	Cycle period [s]
1A	0.157	2.06	157.079
1B	0.206	2.03	157.079
1C	0.103	3.33	245.441

The numerical model was set up with a mesh of 3 by 317 square grid cells. The grid resolution is 0.1 m, so the model effectively covers the flume from the toe of the profile slope ($x = 0$ m) to the end of the constructed profile ($x = 31.7$ m). The measured bathymetry is imposed in the cell centres. This bathymetry was equal for all runs. On the offshore boundary, corresponding to $x = 0$ m in the flume, a water level of 0.0 m was imposed. The maximum still water depth in the flume was 0.75 m. Time series for the short waves and the associated bound long wave were derived in two ways. Firstly, second-order time series were constructed from a Pierson–Moskowitz spectrum using the parameters listed in Table 1, following the methodology outlined in Section 2.3. A standard JONSWAP peakedness factor $\gamma = 3.3$ was judged to be too large when comparing theoretical spectral

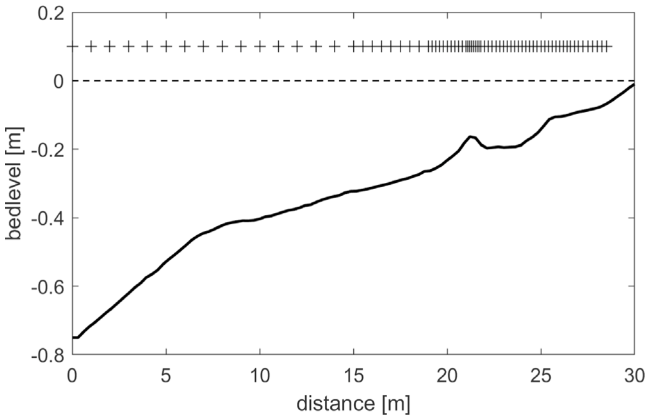

Fig. 4. Flume test bathymetry (solid line), imposed water level (dashed line) and measurement locations (+).

shapes to the measured spectra at the toe of the profile (Boers, 1996). Secondly, first order measured time series were imposed on the model boundary. The associated bound long wave is computed in the model using the formulations of Longuet-Higgins and Stewart (1964). The bed shear stress was imposed using a Chézy parameter of 75 that was uniform over the length of the flume. The model was run for 30 minutes, and output wave height H and water levels ζ were recorded with a frequency of 20 Hz, similar to the flume tests data acquisition. From these time series, the following metrics were derived: setup=$\langle\zeta\rangle$; $Hm0_{HF} = \langle H\rangle$; $Hm0_{LF} = \sqrt{8\,(\zeta_f - \langle\zeta_f\rangle)^2}$, where ζ_f is the low-pass filtered ($f_p/2 - f_p/20$) water level, and H is the modelled significant wave height. $\langle.\rangle$ denotes time averaging over the run duration.

Model results for the measured (M) and spectral (S) input wave time series are compared with the data as measured by Boers (1996). In test 1 A, the setup is overpredicted by the same amount by both runs (Fig. 5(a)). Both M and S runs capture the shoaling and subsequent dissipation of the LF wave in the surf zone (Fig. 5(c)). In test 1B, the M run overpredicts the incident band wave height. In contrast the S run is able to reproduce the linear decrease in the zone seaward of the breaker bar (Fig. 5(e)). Both M and S runs underpredict the LF wave height (Fig. 5(f)). In test 1C, both M and S runs reproduce the setup and the short wave height accurately (Fig. 5(g,h)). The S run slightly overpredicts the LF wave height compared to the M results (Fig. 5(i)). Overall, the model is capable of reliably reproducing the wave height and setup patterns (Table B.2), for both measured and spectral input wave time series. The results are somewhat less precise for the steeper wave conditions characteristic of test 1B.

3.3. DELILAH field experiment

In this section, the focus is on the 2D propagation and dissipation of directionally spread short waves, and the associated forcing of surf zone circulation. More specifically, the implementation of the stationary refraction (“single direction”) approach of Roelvink et al. (2018) will be tested. This approach was designed to counteract the disintegration of modelled wave groups when they are advected over longer distances. In our code, this is done by combining the results of two separate unstructured solvers: the stationary wave module feeds the mean wave direction to the non-stationary short wave driver, which advects the actual wave groups (Section 2.1.4). To this end, we constructed two models, one where we propagate the wave groups using multiple directional bins (MDir), and one where we propagate the wave groups along the mean wave direction only (SDir). We use data of the DELILAH field experiment, held in October 1990 in Duck, North Carolina, at the US Army Field Research Facility (Birkemeier et al., 1997) for verification. Similarly to previous model validation studies (van Dongeren et al., 2003; Roelvink et al., 2009, 2018), the data run of October 13th 1990 from 16:00 to 17:00 was selected. The windless swell conditions were the result of hurricane Lili, and were characterised by a significant wave height H_s of 1.81 m and a peak period T_p of 10.6 s in 8 m water depth. These conditions are energetic enough to generate a significant contribution to low frequency portion of the energy spectrum ($<f_p/2$), and the incident wave spectrum is sufficiently narrow-banded to justify the assumptions in the generation of the wave boundary conditions (Fig. 6(b), Section 2.3). The incident wave angle was 88° from N, corresponding to 16° from shore normal. The local wind conditions were very mild, with a wind speed of 2 m/s from the NE (Birkemeier et al., 1997).

3.3.1. Model setup

The model is set up using an unstructured grid with dimensions of 885 m cross-shore by 700 m longshore. The overall resolution of the grid is 10 m by 10 m, with a local refinement to 5 m in the longshore and cross-shore directions from the edge of the surf zone seaward of station 90 to the coastline. The refinement area covers a longshore distance of 260 m, centred on the measurement transect. The bathymetry in the model is composed of data measured on October 12th and 13th, as the October 13th survey only covered the bathymetry between the dry beach and the surf zone trough (Birkemeier et al., 1997). The bed level data was interpolated in the flow nodes, and the bathymetry was made uniform in the first three rows of cells along the offshore boundary, in order to satisfy the conditions for the validity of the equilibrium theory of Hasselmann (1962). A stationary offshore water level of 0.69 m NGVD was imposed on the offshore boundary. The 2D absorbing–generating boundary was forced with times series generated from the measured spectrum at 8.7 m water depth. The directional spreading factor s of the spectrum is about 6 (Roelvink et al., 2018). The lateral flow boundaries were forced with zero gradient Neumann conditions. We used the Roelvink–Daly breaker formulation (Daly et al., 2012) to calculate energy dissipation through wave breaking. This was shown by Roelvink et al. (2018) to substantially improve the cross-shore variation of the short wave heights and the longshore current in this test case. The breaker parameter γ was set to 0.52, and a Chézy bed roughness value of 65 $\mathrm{m}^{0.5}/\mathrm{s}$ was used. All other parameters were set to their default values. The multiple direction run (MDir, Fig. 7) was run in standard mode, with a directional resolution of 5°. The single direction run (SDir) was set up with that same directional resolution for the stationary wave model. Mean wave directions obtained from the stationary calculation were fed to the surfbeat module every 10 min.

Time series of wave characteristics and water levels were recorded at 1 Hz in the model across a dense cross-shore profile. In order to obtain results that are compatible with the DELILAH dataset, the demeaned water levels ζ were bandpass-filtered to obtain the low-frequency signal ζ_{LF} (0.004 – 0.0495 Hz) and the high frequency signal ζ_{HF} (0.0495 – 0.3 Hz). The corresponding rms LF wave height was then obtained by $H_{rms,LF} = \sqrt{8\,\overline{\zeta^2_{LF}}}$, the rms short wave height $H_{rms,HF}$ as $\sqrt{\overline{H^2_{modelled}} + 8\,\overline{\zeta^2_{HF}}}$, and the longshore velocity as $\langle v\rangle$, with v the cell centre y-component of the Eulerian velocity vector. As our grid is aligned with the coastline, no further rotation is needed.

3.3.2. Results

The groupiness factor GF (List, 1991) was calculated for the SDir (Fig. 7(a)) run and the MDir (Fig. 7(b)) run. The groupiness factor GF is defined as

$$GF = \frac{\sqrt{2\,\sigma^2(H_{rms,HF})}}{\overline{H_{rms,HF}}} \tag{26}$$

where σ denotes the standard deviation. Clearly, the single direction run is able to maintain the wave group structure much better than the multiple directions run. The wave group structure is advected with less

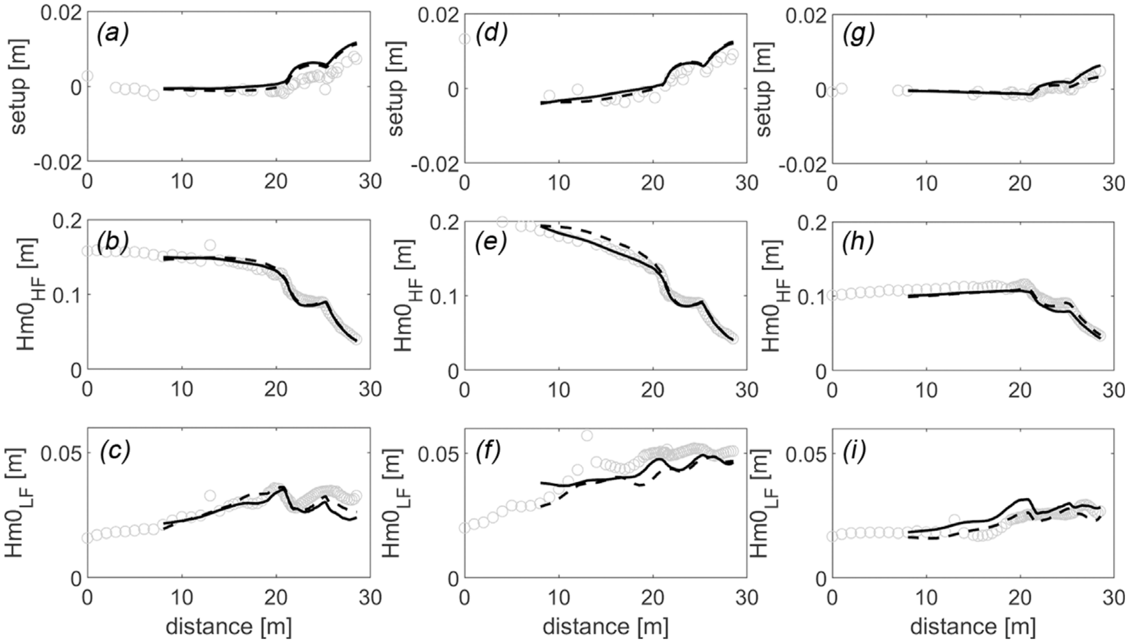

Fig. 5. Boers flume test results. (a)–(c) test 1 A, (d)–(f) test 1B, (g)–(i) test 1C. Top to bottom: setup, $Hm0_{HF}$, $Hm0_{LF}$. Dashed line: measured (M) time series forcing; full line: spectral (S) forcing; dots: measurements.

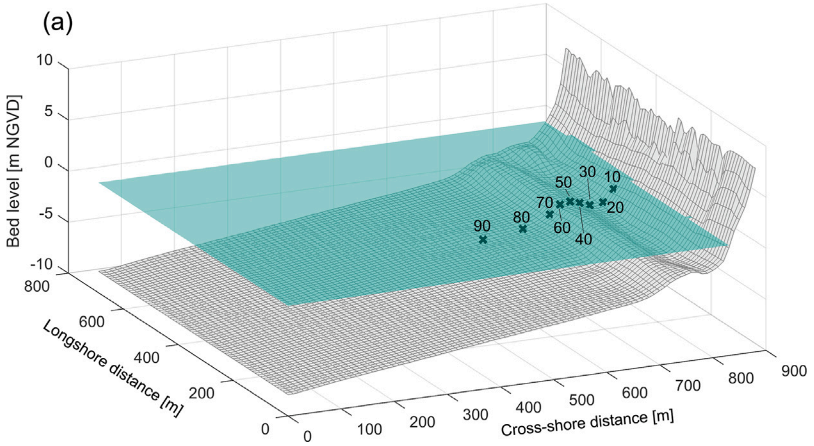

Fig. 6. DELILAH field case geometry. (**a**) The Duck bathymetry on October 13th 1990 featured a linear bar and trough. Crosses indicate DELILAH instrument locations. Coordinates are in the model reference frame. Instrument numbering follows Birkemeier et al. (1997).

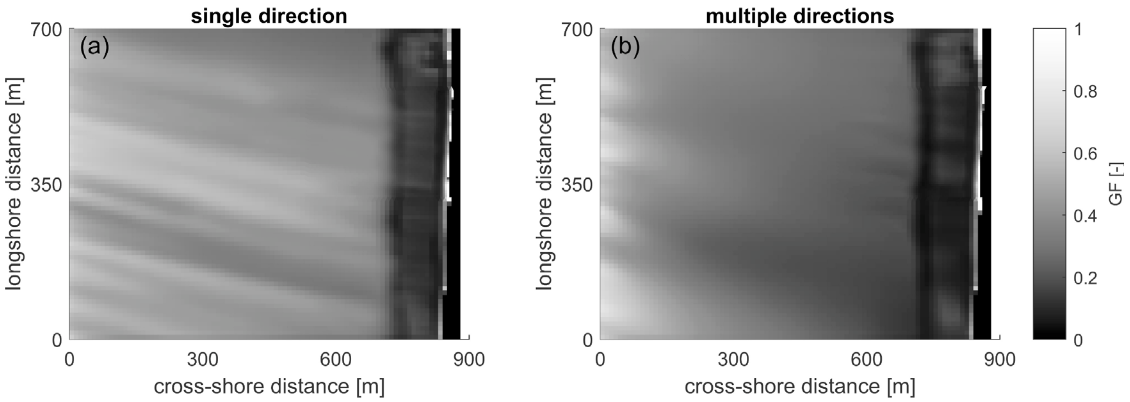

Fig. 7. List (1991) groupiness factor GF for (**a**) the single direction (SDir) run; (**b**) the multiple direction (MDir) run. The wave groups are well defined up until the edge of the surf zone for the SDir run. In contrast, the MDir run loses the wave group structure quickly away from the offshore boundary.

numerical dissipation up until the edge of the surf zone, with improved surf zone LF wave heights as a result (Fig. 8(c)).

The cross-shore evolution of the HF wave height, the LF wave height and the longshore current velocity obtained from the two runs were compared to the measured data (Fig. 8). Both the MDir and the SDir run capture the short wave height distribution and dissipation in the surf zone well, although the shoaling process seaward of the sandbar is underestimated by both models. Moreover, neither model captures the wave energy dissipation between stations 20 and 10 (Fig. 8(b)). The LF wave height is simulated well using both SDir and MDir approaches, compared to previous results of Roelvink et al. (2009, 2018) in XBeach. The SDir run reproduces the LF wave height distribution in the surf zone better. Only the shoreline value (station 10) is overestimated, but the overall pattern and magnitude match well with the data (Fig. 8(c)). This finding is corroborated by the low frequency spectrum plots in Fig. 9. The LF energy modelled in the SDir and MDir runs generally corresponds well to the measurements, except in stations 10 and 70, where the LF energy is overestimated around the peak IG frequency. The peak longshore velocity is underestimated by both runs by about 30% (Table B.4). The longshore current distribution and magnitude proved to be extremely sensitive to the spatial and directional grid resolution of the model. When using comparable settings as Roelvink et al. (2018), the model underpredicted the current velocity magnitude with an error of 75%. Overall, the model is reproducing the HF and LF wave patterns well, with the standard settings for the bottom roughness (Chézy value of 65 $\mathrm{m}^{0.5}/\mathrm{s}$) that we have used here (Table B.4). Regarding performance, the use of unstructured grids allowed a reduction of the number of grid cells with 65 % compared to a run on full 5 by 5 m resolution, reducing the runtime with a factor 2.2 for the MDir setup. Using the stationary refraction approach, this improved further to a factor 5.9, with the added benefit of better preservation of the wave group structure, and slightly better LF wave height prediction in the surf zone.

3.4. COAST3D Egmond field experiment

The COAST3D Egmond field case aims at reproducing the hydrodynamics during a storm event in a double barred nearshore area, when local IG wave generation was important. The beach experiments in Egmond aan Zee were part of a multi-institution set of field campaigns in the Netherlands and the UK in 1998–1999 within the framework of the EU MAST–III funded COAST3D project (Soulsby, 2001). The aim of the project was to collect a comprehensive dataset of hydrodynamic and morphological observation that would allow to test the accuracy of morphodynamic models under field conditions. The mesotidal beach and nearshore at Egmond feature an intertidal swash bar and two offshore breaker bars, that are intersected by rip channels. In this test case, we use data from the main campaign in October–November 1998. During this field experiment, an large array consisting of 32 stations intermittently measured waves, currents, water level and bed dynamics throughout a number of storms (Ruessink, 1999). Breaker bar movement was tracked 22 times during the field campaign up until NAP -6 m with DGPS positions of a 15 m high amphibious buggy called WESP, that drove cross-shore tracks at alongshore intervals of about 50 m. The deeper parts of the nearshore were measured once before the main campaign on September 1st 1998, using a hydrographic vessel of Rijkswaterstaat (Klein et al., 2001).

Hydrodynamic data is available from an array of pressure sensors located on the inner breaker bar (stations 1A–1D, 7B, 7E), and a pressure sensor on the outer bar (station 2, Fig. 11(a)). The deep water wave conditions during the field experiment were measured by a directional waverider buoy (station 8), located in 15 m water depth, about 5 km offshore of the field site. Comparison with nearby operational wave measurement locations of Rijkswaterstaat showed insignificant wave energy dissipation between stations deeper than 30 m and the location of station 8, and any gaps in the station 8 time series were reconstructed using these ancillary wave data (Vermetten et al., 2001). Tide levels at the field site were derived from the tide gauges at IJmuiden and Den Helder (Ruessink et al., 2001).

The selected depth, short and infragravity wave data were recorded on October 25th 1998 between 01:00 and 13:00 GMT, and cover one tidal cycle (Fig. 10). This time frame corresponds to the first storm peak during the measurement campaign. Tidal water levels vary between −0.4 and 1.75 m NAP, the significant wave height at station 8 varied between 3.0 and 4.2 m. Wave peak period were between 8.7 and 9.8 s. Notably, over the course of the tide, the incident wave angle shifted from SW to NW. The last available WESP bed level measurements before the storm were recorded on October 24th 1998, and were used in the model setup.

3.4.1. Model setup

The model grid is a progressively refined unstructured grid of 2500 m in the longshore and 1600 m in the cross-shore direction, aligned with the local coastline orientation. The grid resolution at the offshore boundary is 20 m, onshore of the −8 m contour and toward the centre of the domain the resolution is 10 m, and onshore of −6 m around the observation stations, the resolution is further reduced to 5 m (Fig. 11). This choice of resolution allows to accurately capture the wave group propagation and dissipation processes, resulting in a grid of 32286 cells . The model was set up in multi-directional mode with a directional resolution of 5°. To compensate for the difference in cross- and longshore bed level data availability and to avoid triangulation artefacts, the WESP track data of October 24th were converted to a bed level sample set using the methodology of Thanh et al. (2020), and subsequently interpolated on the unstructured grid cell corners. Bathymetry in areas not covered by the WESP measurements was interpolated from the offshore bed level data of September 1st 1998, and from the regular monitoring dataset of the Dutch government (the so-called Vaklodingen). The boundary conditions were taken from Vermetten et al. (2001). Wave boundary conditions were imposed as a time series of hourly parametrised JONSWAP spectra with a peakedness and cosine spreading factor of 2.4 and 4, respectively. The wave buoy at station 8 malfunctioned after October 25th 2:00, and the remainder of the time series of wave bulk parameters was derived from the operational buoy network data of Rijkswaterstaat by wave height class dependent interpolation (Vermetten et al., 2001). The offshore model boundary is a 2D absorbing–generating boundary forced with the tidal water level and the IG volume fluxes. By calibration on the data of October 25th 1998 09:00 (Table B.5), the bed roughness was fixed at a global Chézy roughness parameter of 65 $\mathrm{m}^{0.5}/\mathrm{s}$. We applied the Daly et al. (2012) wave breaking formulation with a gamma value of 0.48 and alpha 1.1. The roller model was switched on, with the roller slope set to 0.1. Wave–current interaction was switched off. Any other parameters were left to their defaults. The model was then run on 6 parallel partitions for the 13 h model validation period.

Model results are extracted as time series at the instrument locations where pressure data was available for the entire duration of the model run. Modelled data were saved at a frequency of 2 Hz, and hydrodynamic parameters are calculated from 1800 s bursts over the frequency bands reported in Ruessink (1999) in order to match the field data. The demeaned water levels ζ were bandpass-filtered to separate the low-frequency signal ζ_{LF} (0.004–0.05 Hz) from the high frequency signal ζ_{HF} (0.05–0.33 Hz). The corresponding rms LF wave height was then obtained by $H_{rms,LF} = \sqrt{8\,\overline{\zeta_{LF}^2}}$, the rms short wave height $H_{rms,HF}$ as $\sqrt{\overline{H_{modelled}^2} + 8\,\overline{\zeta_{HF}^2}}$.

3.4.2. Results

Water depth and $H_{rms,HF}$ are well reproduced by the model in all the observation points, except in station 7B (Fig. 12). Cross-shore wave dissipation patterns are well modelled over the course of the tidal cycle. The rms error in the estimates of both parameters is smaller than

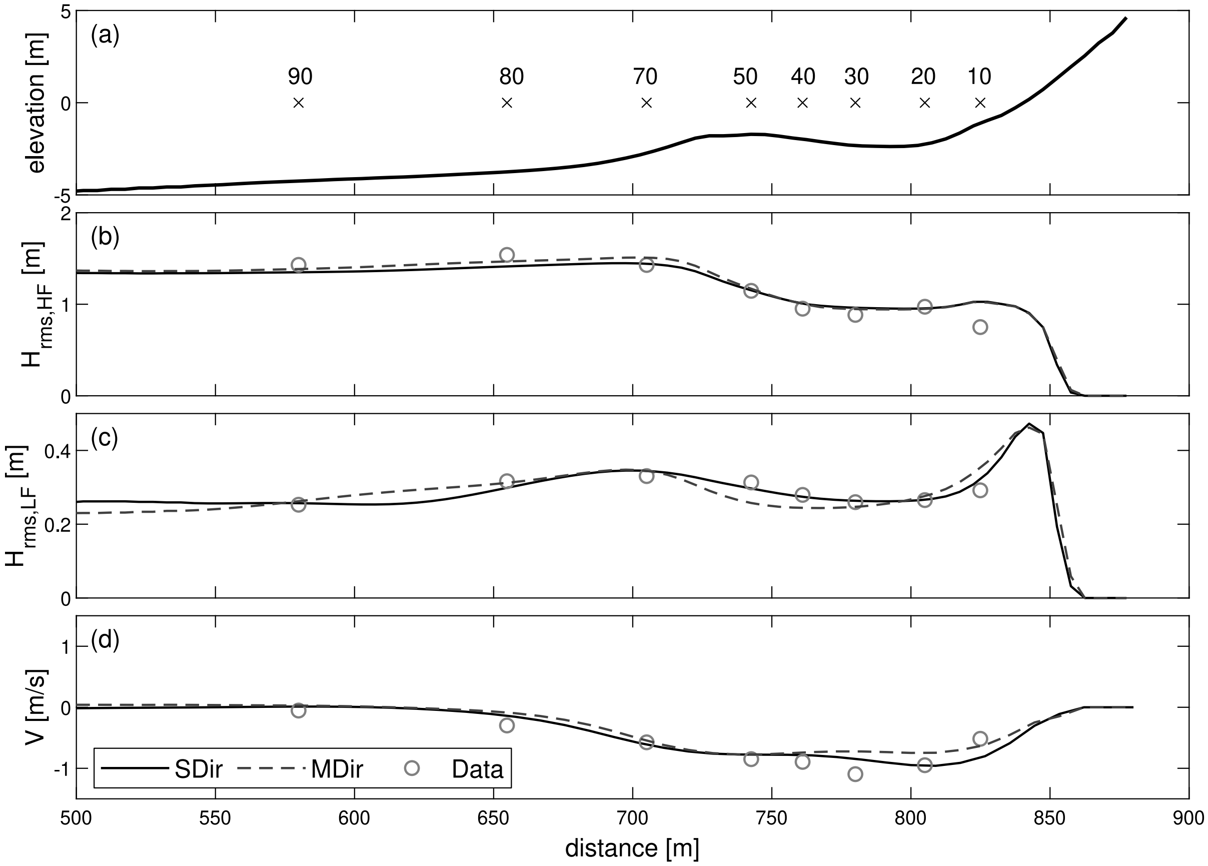

Fig. 8. Cross-shore distribution of (**a**) model bathymetry and DELILAH measurement locations (Birkemeier et al., 1997); (**b**) short wave height $H_{rms,HF}$; (**c**) low frequency wave height $H_{rms,LF}$; (**d**) longshore velocity v.

10 % of the observed value (SCI, Fig. 12(a–n)). Both water depth and HF wave height are systematically overestimated. All model errors are within the bounds of the measurement errors, estimated at $0.05-0.15$ m for the water depths, and ∼15% for the HF wave heights in breaking wave conditions (van Rijn et al., 2000). Moreover, the water depth bias is in the order of the measurement uncertainty of the bottom level data as reported by van Rijn et al. (2000). In station 7B, the water depth is on average overestimated by 0.22 m, and the wave height by 0.3 m. The position of station 7B is aligned with a rip channel through the inner breaker bar, which may explain part of the discrepancies between model and data. The nature of the available bed level data does not allow to accurately resolve the alongshore bed level variability required to reproduce the rip channel geometry, so the model bathymetry may be too deep at that location. The larger water depth then allows for larger wave heights under breaking wave conditions. This however would only allow an overestimation of around 0.1 m, given the maximum permissible wave height over water depth ratio of 0.48. We likely underestimate the wave breaking on the outer bar (onshore of station 2), yielding larger wave heights in the trough between the outer and the inner bar. Further evidence in this direction is that according to the data, waves in station 7B are never breaking ($H_{rms,HF}/h \leq 0.35$ throughout the tide), while the waves in the model do break ($H_{rms,HF}/h \approx 0.45$ throughout the tide). However, we have no data on the outer bar top to verify this. Although station 7B is close to a rip channel, the lack of wave–current interaction in our model does not play a role in the overestimation of the wave height, as that would yield an opposite effect (Weir et al., 2011).

The comparison between modelled and measured $H_{rms,LF}$ values shows substantial scatter, but the model error is generally expected to deviate 20 % or less from the observed values (SCI, Fig. 12(o–u)). Error metrics for the LF wave height in station 7B show values that are comparable with those of the other observation stations. In order to explain part of this scatter, we inspected the spectra of stations 2 and 1A–D on October 25th 1998 07:00 (Fig. 13). These spectra show that the IG peak period is predicted reasonably well, and that the IG energy around the IG spectral peak is overpredicted. The model however underpredicts the energy content for IG frequencies higher than 0.025 Hz. A factor playing a role in this underprediction is the absence of free long waves in the boundary forcing. A bispectral analysis of the water level data in station 2 for this burst, and using the method of Herbers et al. (1994) (their eq. 5 and 6), reveals that approximately 49% of the total IG energy content was directly forced by wave groups. The remaining 51% is free IG energy, that originates from outside the model domain, or from local reflection off the coastline.

Overall, this field case demonstrates that the model can reliably reproduce the hydrodynamic conditions in a multi-bar system during an energetic wave event. Water depths and short wave fields are simulated to within measurement accuracy, while the IG wave height is mostly underpredicted due to the lack of a mechanism to transfer energy between HF and LF bands in the shoaling and outer surf zone, and because of the missing free long wave contribution in the boundary forcing. Regarding efficiency, a comparable XBeach model with the same 5 m resolution over the surf zone has a grid size of 51712 cells (factor 1.6 higher), and ran with a timestep of 0.11 s (45% smaller for the same CFL value of 0.7).

3.5. PILOT field experiment

In this verification case, we have tested the parallel implementation of the surfbeat model on the 2D field case of a fringing reef in Guam, which is a challenging study area featuring longshore bathymetry variability with very steep gradients, a narrow surf zone and large bottom roughness. The PILOT field experiment is a long term deployment

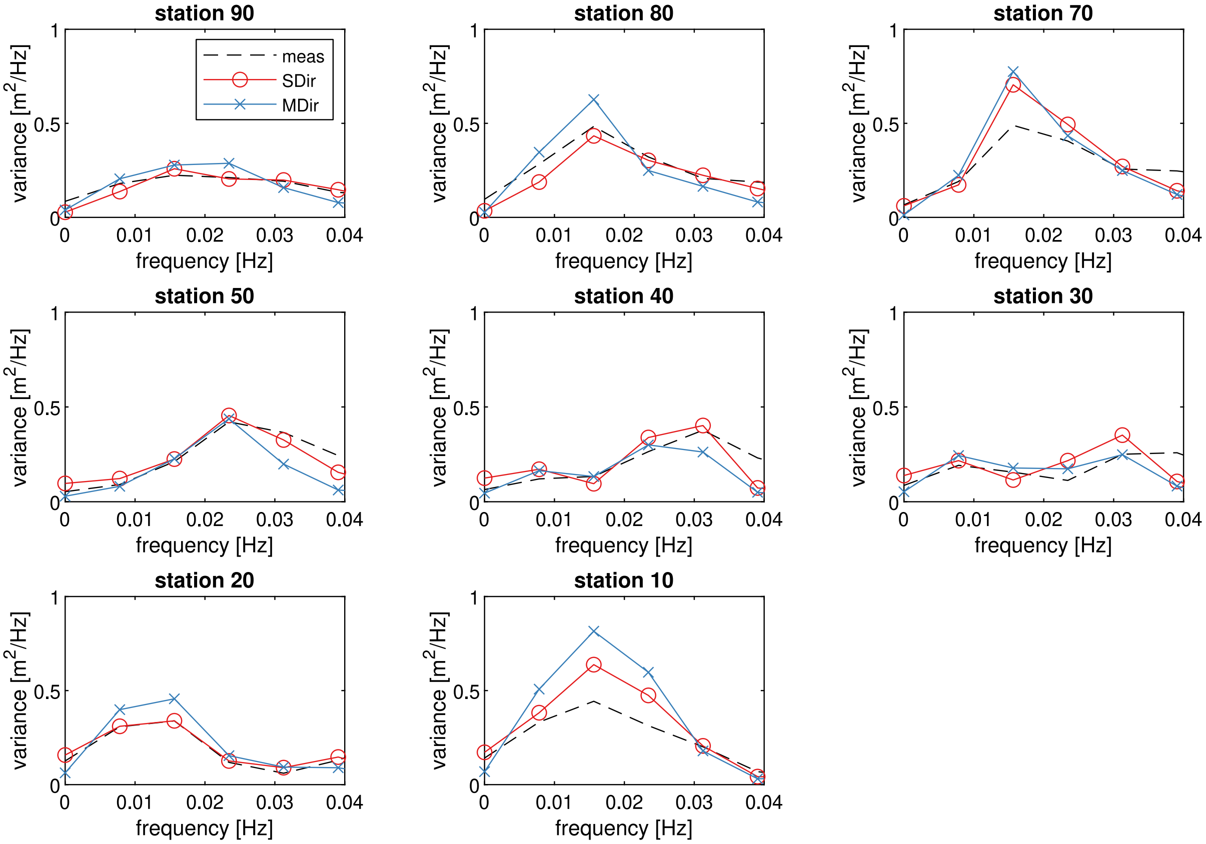

Fig. 9. Measured and modelled LF spectra DELILAH field case. Spectra were calculated at a 0.01 Hz resolution using a Hanning window, with a 50% overlap. Red dots: SDir run; Blue crosses: MDir run; Black dashed: measurements (Birkemeier et al., 1997). Note that there is no data available for station 60.

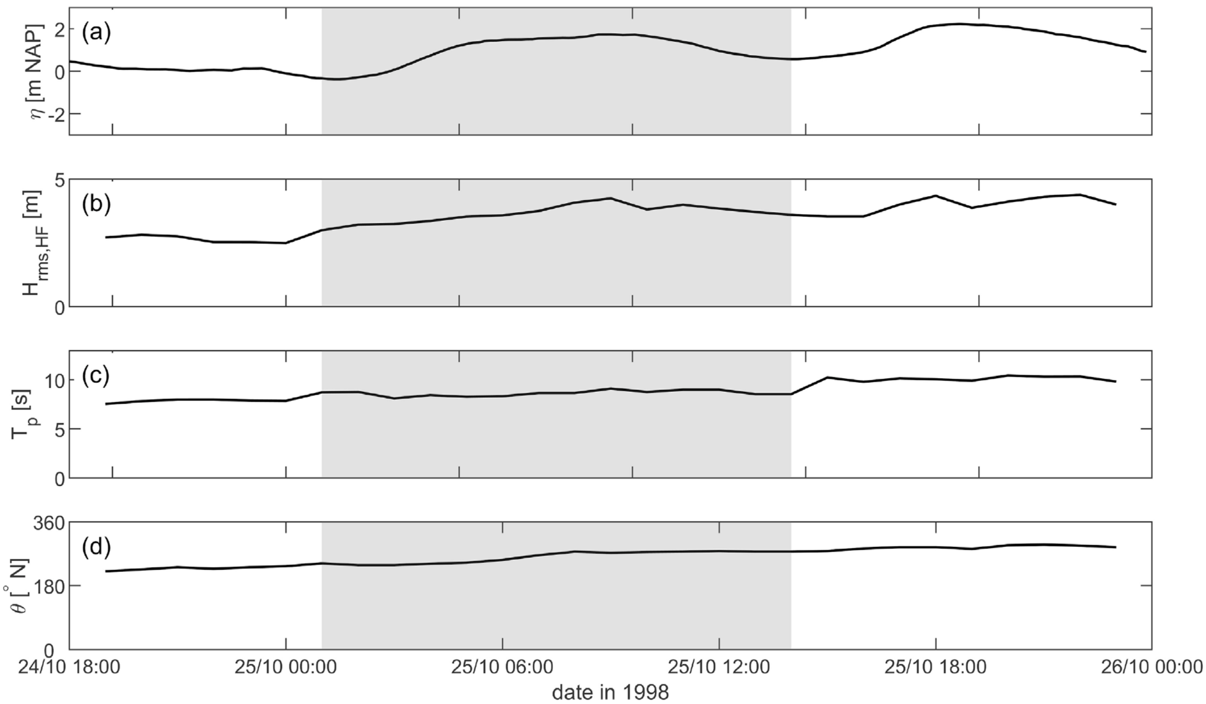

Fig. 10. COAST3D model boundary conditions. The vertical grey bar indicates the modelled time period, October 25th 1998 between 01:00 and 13:00 GMT. (**a**) Tide relative to the Dutch NAP vertical reference level; (**b**) RMS wave height; (**c**) Peak wave period; (**d**) Wave direction.

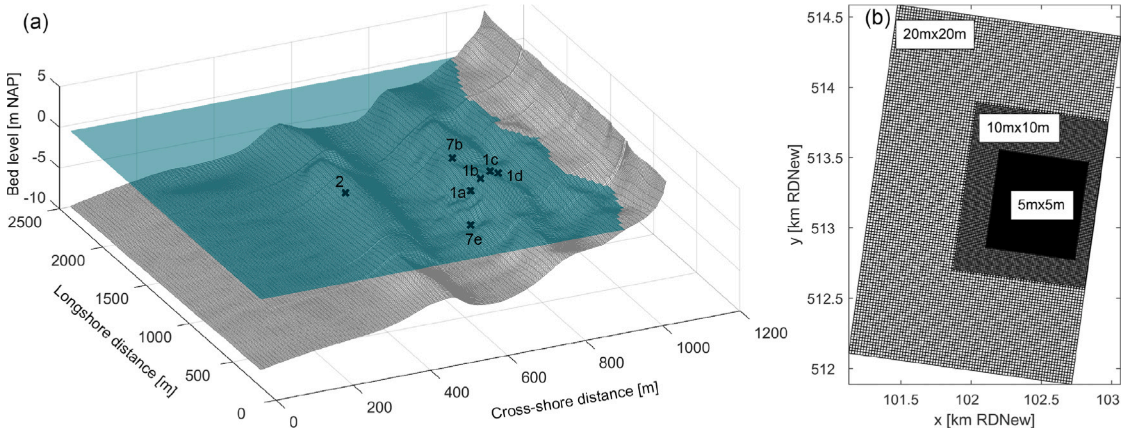

Fig. 11. COAST3D model setup. (**a**) Bathymetry and measurement locations on October 24th 1998. Bed level values are relative to the Dutch NAP vertical reference level; (**b**) Model grid with local flexible resolution adaptations. Coordinates in the Dutch RD New system.

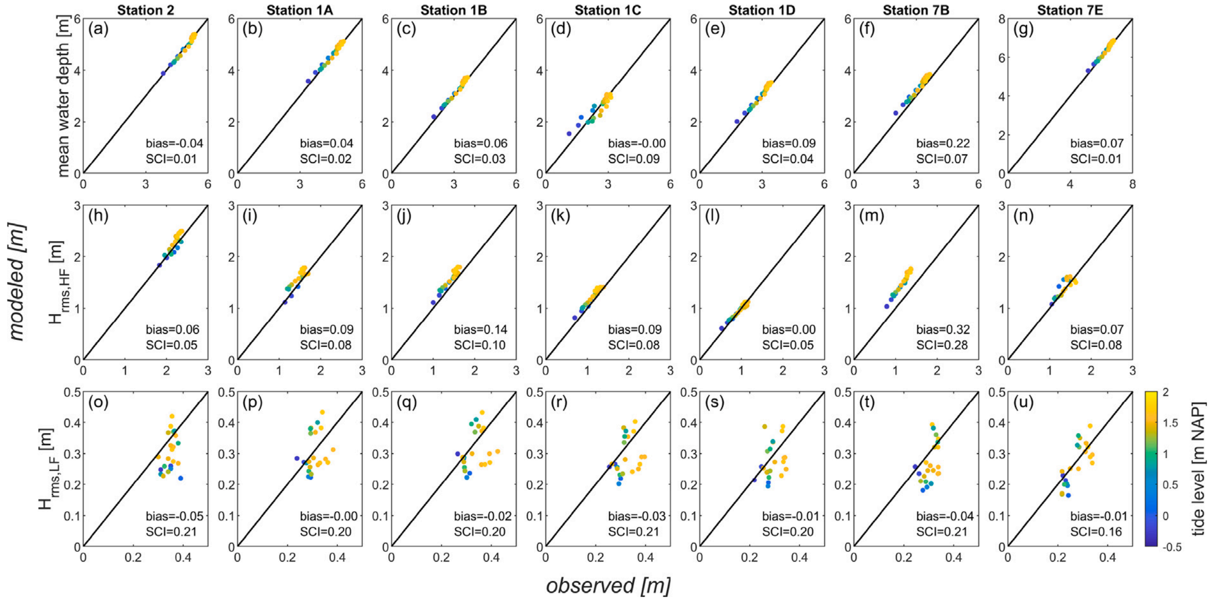

Fig. 12. COAST3D model results for October 25th 1998, 01:00 to 14:00 GMT. (**a–g**) Water depth; (**h–n**) Short wave H_{rms} (0.05–0.33 Hz); (**o–u**) Low frequency H_{rms} (0.004–0.050 Hz). The colour of the dots indicates the offshore tidal level. Station locations are indicated in Fig. 11(**a**).

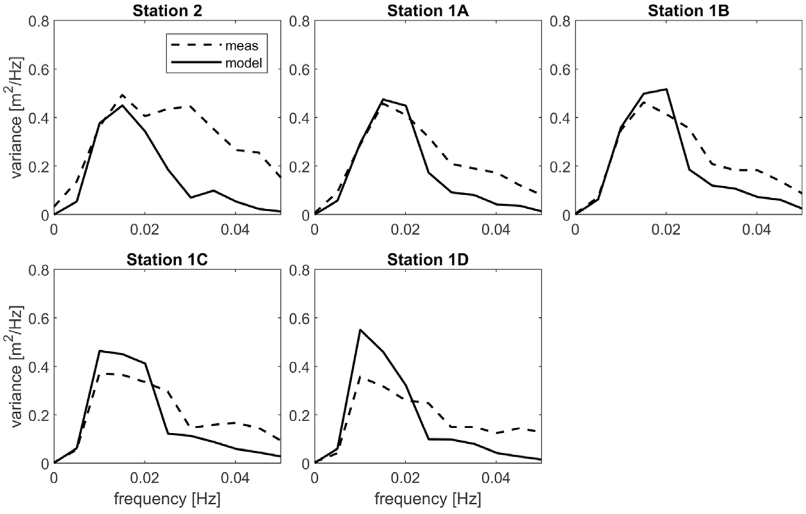

Fig. 13. Measured and modelled LF spectra COAST3D field case. Spectra were calculated from 1800 s bursts at a 0.005 Hz resolution using a Hanning window, with a 50% overlap. Full line: model results; Dashed line: measurements (Vermetten et al., 2001).

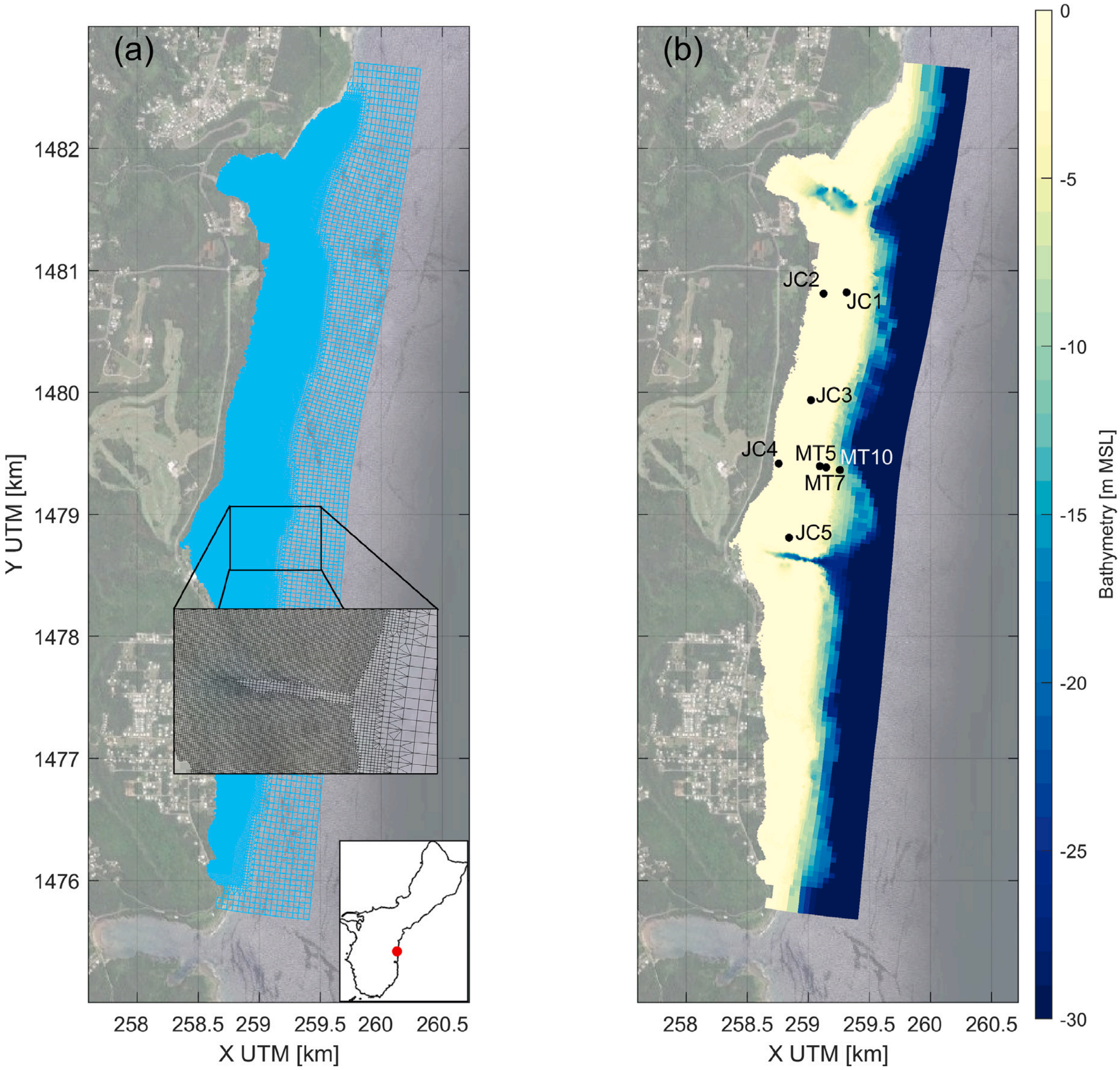

Fig. 14. PILOT model setup. (**a**) Model grid with local flexible resolution adaptations; (**b**) Bathymetry and measurement locations.

(2005-present) of a number of measurement arrays of pressure sensors and current meters in varying reef environments. One of the field sites is at Ipan, on the SE coast of Guam (Péquignet et al., 2009; Vetter et al., 2010; Péquignet et al., 2014; Clark et al., 2020). The reef is situated between two small headlands, and it is about 7 km long and ~ 400 m wide. It is incised by two cross-reef channels up to 30 m deep (Fig. 14(b)), which drain small watersheds. The reef flat is fairly featureless, consisting of algae-covered coral with interspersed sandy patches. The reef crest is more shallow and rougher. The reef front is very steep, and features spur-and-groove morphology (Péquignet, pers. comm., Clark et al. (2020)). The selected data was recorded on January 10th 2012 between 7:00 and 7:30, by an array of Seabird SBE26 pressure sensors (MT5, MT7, MT10, JC2, JC5) and Aquadopp velocity profilers (JC1, JC3, JC4) (Becker, pers. comm., Fig. 14(a)). The offshore Hm0 measured by Coastal Data Information Program (CDIP) buoy 121, located in 200 m water depth, 2 km SE of the study site, was 3.18 m, with a T_p of 10.5 s incoming from 56° N. The spectrum is narrow-banded, so it is suitable for our approach to generate wave boundary conditions (CDIP, 2021). The wind velocity measured in the nearby Pago Bay NOAA station 1631428 (NOAA, 2020) was 3.0 m/s, coming from 48° N. The offshore tidal level was 0.3 m w.r.t. MSL (Section 3.5.1).

3.5.1. Model setup

The grid and the bathymetry of the model need to fulfil several requirements for this case. The area has a very shallow reef flat (~0.5 m below MSL), fronted by a steep reef front that quickly drops to depths of more than 50 m. The cross-reef channels are ~30 m deep. The wave breaker zone is narrow, but should be captured at high resolution to model the wave energy dissipation profile correctly, as this dissipation forces wave setup and wave driven currents. The offshore area on the other hand, should be modelled with only enough detail to resolve the structure of the wave groups. The fine resolution needed in the breaker zone should not affect the offshore part of the grid, neither should this refinement be used around the reef channel, to minimise CFL-based time step restrictions. After several tests, the offshore grid resolution was fixed at ~35 m, the reef front area is refined up until ~5 m, and the reef flat is kept at the same ~5 m resolution. At the location of the cross-reef channels, the grid is derefined to 10 m to alleviate time step restrictions (Fig. 14). The final unstructured model grid has 121,989 flow nodes, and was run on 20 parallel domains.

The bathymetry used in the model was collated from 2 datasets. The JALBTCX Topobathy Lidar dataset (NOAA, 2018) provided data on the reef flat at 1 m resolution or better. Offshore areas not covered by this Lidar data were filled using the Guam 1/3 arc-second MHW

Coastal Digital Elevation Model (NOAA, 2008), a 10 m resolution dataset for tsunami modelling. Both datasets were referenced to MSL, and interpolated to the flow nodes of the model grid. The offshore depths were limited to a maximum of 30 m, to reduce potential timestep restrictions. As second-order long wave forcing is expected to be very small in these depths, we do not expect significant deterioration of the results. A spatially varying field of Chézy roughness parameter values was constructed based on the satellite derived Benthic Habitat Map of Guam (NCCOS, 2004), where coral patches got a roughness of $40\,\mathrm{m}^{0.5}/\mathrm{s}$, and sand patches and algal turfs a roughness of $50\,\mathrm{m}^{0.5}/\mathrm{s}$. This is somewhat less than the roughness derived by Clark et al. (2020), which would correspond to a roughness of about $31\,\mathrm{m}^{0.5}/\mathrm{s}$, but it corresponds well with the value of $\sim 40\,\mathrm{m}^{0.5}/\mathrm{s}$ obtained by Vetter et al. (2010) by doing a cross-shore momentum balance during energetic conditions. The wave friction factor, which was shown previously to be important on reefs (van Dongeren et al., 2013), was set to 0.45, which is somewhat less than the value of 0.60 used by van Dongeren et al. (2013) to model reef circulation in Ningaloo, Australia. The model was run with wave–current interaction switched on, as the cross-reef channel outflow is likely to have an effect on the local short wave propagation.

Initial runs forced with CDIP-only wave data consistently resulted in overestimation of the wave heights in the model. As such, wave height and period on the offshore boundary were taken from measurement location MT10 at 8 m water depth, and only the wave direction from CDIP buoy 121. The wave height at the buoy is typically 130% of the MT10 value. In order to derive an offshore water level boundary signal, a regional tide model was constructed, forced with TPXO8 data (Egbert and Erofeeva, 2002). The tidal model was calibrated on tidal constituents at the Pago Bay (station 1631428, just N of our study site), and Apra Harbor (station 1630000) NOAA tide gauges (NOAA, 2020). To explore the necessity of including potential larger scale water level forcing, non-tidal residuals (NTR) at the Pago Bay station were determined from the measured time series at the NOAA station using a Godin filter (Thompson, 1983). The NTR's were found to correlate highly with the incident wave conditions measured at station MT10 ($R^2 = 0.66$, not shown), indicating the dominant influence of wave setup on the reef flat next to the tide gauge on semidiurnal and longer time scales. As such, the NTR's were not taken into account in constructing the offshore water level boundary conditions, as wave setup/setdown is resolved in the model. Local wind direction and wind speed were sourced from nearby NOAA measurement station Pago Bay (station 1631428, NOAA (2020)).

3.5.2. Results

Comparison of the model results with the measured data of Clark et al. (2020) on January 10th 2012 at 7:00 shows that the short wave height $Hm0_{HF}$ is well reproduced in the deepest observation point MT10, indicating little energy loss in the model between the deeper part of the domain and the shoaling zone (Fig. 15(a)). The overestimation of $Hm0_{HF}$ at station MT7, and the underestimation at MT5 demonstrate a somewhat too large dissipation in the breaker zone. The short wave energy is almost completely dissipated shoreward of the breaker zone, as evidenced by stations JC2 and JC5. This is well reproduced in the numerical results. The model is able to simulate the low frequency wave height $Hm0_{LF}$ trend in the cross-shore direction fairly well (stations MT10–MT5, Fig. 15(b)), but the low frequency wave height is overestimated toward the cross-reef channel in the middle of the site (station JC5), and toward the northern end of the reef flat (station JC2). In Fig. 15(c), the comparison between the modelled and the measured mean water levels, taken as the sum of the offshore tide level and the steady wave setup, is shown. Both the cross-shore trend (stations MT10–MT5; JC4) and the longshore trend (JC1, JC3, MT5, JC5) are well reproduced.

Comparison of the water level variance in the low-frequency band (0.0011–0.0400 Hz) between the model and the measured data shows that the model is capable of simulating the bulk low-frequency wave heights $Hm0_{LF}$. Moreover, it has some skill in reproducing the energy repartition over the frequencies in the 0.0011–0.0400 Hz band in this field case (Fig. 16). The model somewhat underestimates the variance at frequencies higher than 0.02 Hz, and overestimates the energy content at frequencies below that threshold, especially at station JC2. As in the COAST3D case, it is unknown what the amount of free IG wave energy is, that is entering the model domain through the boundaries, and that could contribute to the model-data discrepancy we observe.

Under stationary conditions, ignoring wind stress and lateral exchange of momentum, the depth-averaged conservation of momentum in the cross- and alongshore directions on the reef can be written as a balance between water level gradient, wave forces and bottom friction:

$$g\frac{\partial \zeta}{\partial i} - \frac{F_{w,i}}{\rho(h+\zeta)} + \frac{\tau_{bottom,i}}{\rho(h+\zeta)} = 0 \quad i = x, y \tag{27}$$

in which F_w is the wave force, h is the mean water depth, τ_{bottom} represents the bottom shear stress, and x and y represent the cross- and longshore directions, respectively.

The cross- and longshore momentum balance of the Ipan reef on January 10th 2012 07:00, was analysed based on a 30 min time-average (Fig. 17). For the modelled conditions, we find strong seaward currents through the two incised stream channels that cross the reef, and through local depressions in the reef crest (Fig. 17(d)). Gradients in wave setup are steep throughout the narrow surf zone, where almost all the SS wave energy is dissipated through intense breaking (Fig. 17(a,b)). On the reef flat proper, cross-shore radiation stress gradients are virtually non-existing, leading to limited cross-shore setup gradients that are balanced by cross-shore flows, as evidenced by the bed shear stress patterns (Fig. 17(c,d)). On the reef flat, the current patterns are defined by the positions of the deep cross-reef channels (Fig. 17(h)). At those channels, cross-shore wave setup is locally reduced, as there is relatively less dissipation by depth-induced wave breaking (Fig. 17(b)). This leads to the development of the alongshore setup gradients that were reported by Clark et al. (2020). As steady wave setup is relatively uniform across the reef flat toward the shore, a flow develops over the reef flat toward the channels (Fig. 17(g,h)).

In this field case, we simulated the propagation of a swell field onto a fringing reef flat. We were able to reproduce the wave height distribution over the reef flat. The local grid resolution adaptations clearly demonstrate the advantage of the present modelling approach as opposed to a curvilinear model like XBeach (Roelvink et al., 2009). An equivalent XBeach model needed ~370,000 cells to resolve the reef flat hydrodynamics at the same resolution, using a maximum time step that was 40% smaller for the same CFL number of 0.7.

3.6. Buck Island case

The final verification case explores the capabilities of the model to replicate the propagation of wave groups over larger distances in a topographically complex area, using multiple MPI domains and local grid refinements, with boundary conditions derived from a large scale regional model based on global wave data. Buck Island Reef National Monument (BIRNM) is located on the north-east coast of St.-Croix island, part of the US Virgin Islands in the Caribbean Sea (Fig. 18). The island coastline is protected from incoming swell waves from the Atlantic Ocean by the sequence of a narrow barrier reef complex surrounding the island to the NW–NE, and a shallow fringing reef surrounding the island's coastline. The reefs are separated by a ~10 m deep lagoon characterised by the presence of coral bommies, which locally enhance the hydraulic roughness. Depths in the reef system vary between 1.0 and 15.0 m. Two multi-month deployments in 2015 and 2016 of 8 RBRsolo pressure transducers on cross-shore transects over the fringing reef collected water level and wave data (Rosenberger et al., 2020a). The raw pressure data was collected in bursts of 2048 s

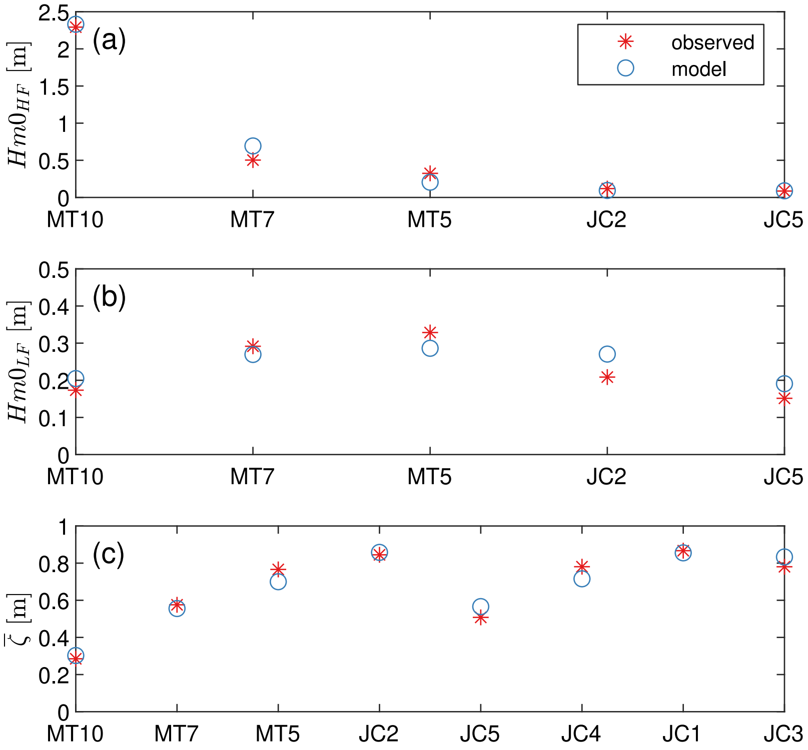

Fig. 15. Model-data comparison PILOT model for January 10th 2012 07:00. Red: data from Clark et al. (2020); Blue: model results. (**a**) short wave $Hm0_{HF}$ (0.04 Hz–0.3 Hz); (**b**) low frequency $Hm0_{LF}$ (0.001 Hz–0.04 Hz); (**c**) water level $\bar{\zeta}$. For station locations, see Fig. 14(b).

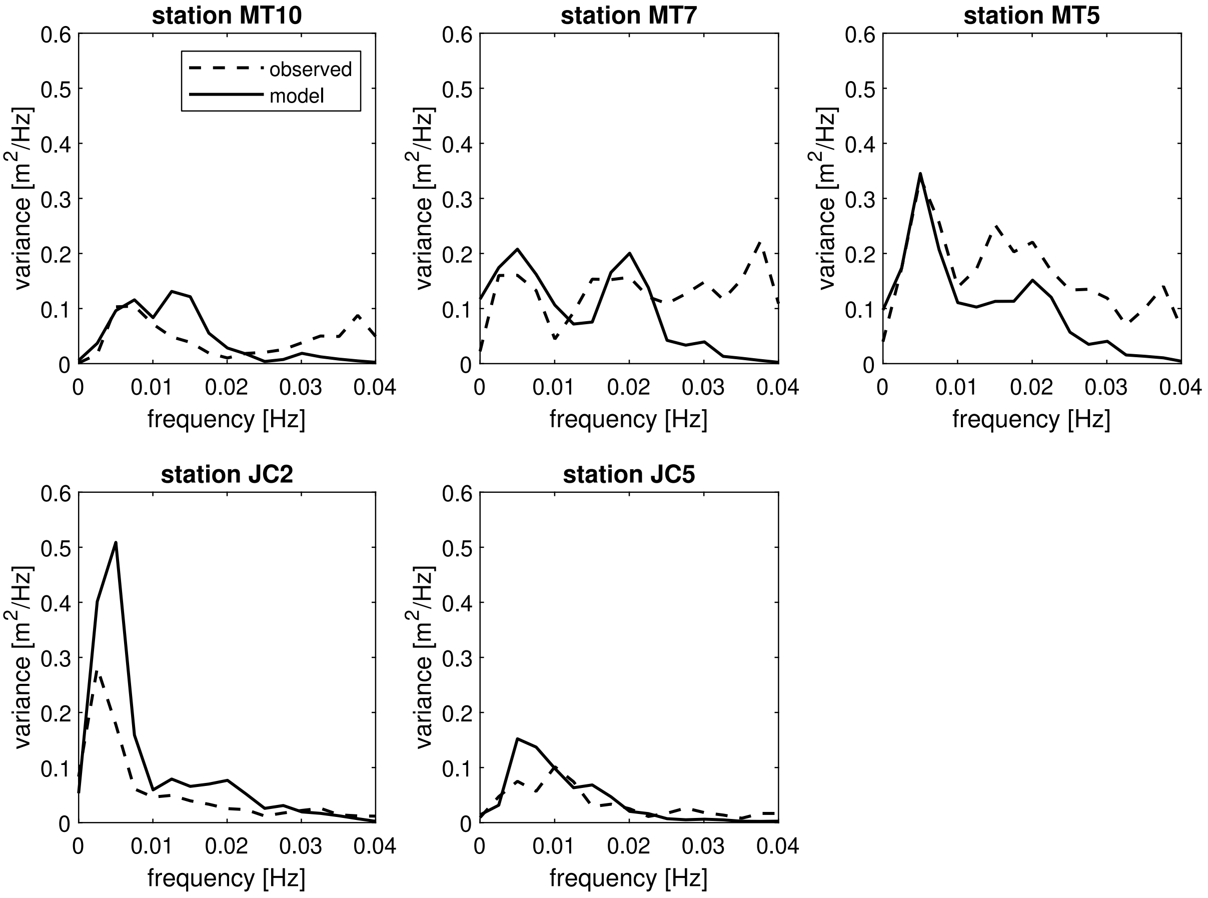

Fig. 16. Low frequency spectra (0.0011–0.0400 Hz) on January 10th 2012 07:00 at Ipan, Guam. The spectra were calculated using a Hanning window with 50% overlap, and a spectral resolution of 0.0025 Hz. Station names correspond to the locations in Fig. 14(b).

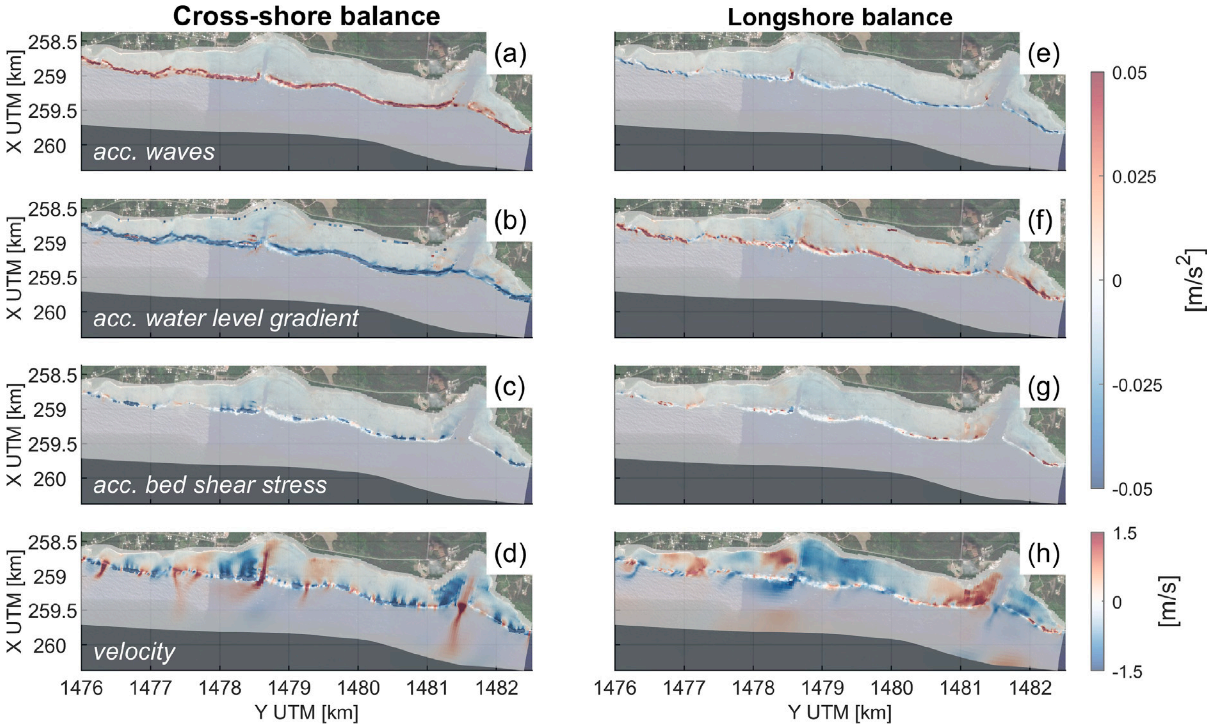

Fig. 17. Cross- (**a–d**) and longshore (**e–h**) momentum balance on January 10th 2012 07:00 at Ipan, Guam. (**a,e**) radiation stress term; (**b,f**) water level gradient term; (**c,g**) bed shear stress term; (**d,h**) resulting mean GLM velocity field. The shore-normal direction is taken as 100°N. Positive cross-shore direction is offshore directed, positive longshore direction to the N. Incident wave direction is 56°N.

every hour at 2 Hz. To verify our model results, we use the data collected between January 12th 2016 18:00 and January 13th 2016 18:00 GMT, the largest measured swell event during the field campaign in the winter of 2015, in observation points N1–N4 on the northern fringing reef of the island (transect N, Fig. 18(b)) and S1–S4 (transect S, Fig. 18(c)) covering the southeastern fringing reef. Conditions during this time frame were characterised by small tidal water level variations between −0.05 m and 0.15 m w.r.t. MSL. The swell event, characterised by waves of around 2 m height with a peak period varying between 10 and 12 s, was impinging on the island from the NE. The northern N transect was directly exposed to this swell, while the wave field had to refract around the island to reach transect S.

3.6.1. Model setup

In order to resolve the various spatial scales involved in the propagation, refraction and dissipation of the wave field, a grid was constructed with several degrees of resolution refinement using similar considerations as for the PILOT case. The offshore part, where short waves do not dissipate, and the propagation of long waves is important, has a resolution of 30 m. The same holds for areas that do not directly influence the hydrodynamics measured in the two transects (Fig. 18(a), zone A). Over the shallower barrier reef and the lagoon (Fig. 18(a), zone B) the resolution is increased to 15 m. The fringing reef area (Fig. 18(a), zone C) has a resolution between 7 and 3 m, in order to resolve short wave dissipation and IG generation by breakpoint forcing, typical of reef lined coasts (Pomeroy et al., 2012; Péquignet et al., 2014). The final number of grid cells is 50999. The directional resolution was set to 5°. Similarly as for the PILOT case, the bed levels used in the model were sourced from 2 datasets. The high resolution USGS EAARL-B topo-bathymetric Lidar dataset for St.-Croix (Fredericks et al., 2015) was used to interpolate the bathymetry in the fine resolution parts of the grid, where large bathymetric gradients occur over limited spatial scales. The grid parts not covered by the Lidar dataset were filled with 1/3 arc-second MHW Coastal Digital Elevation Model data for the US Virgin Islands (Love et al., 2015). Bed level data was reduced to MSL using the tidal benchmark data of the Christiansted Harbor NOAA station (NOAA, 2022). The offshore depths N of the barrier reef were limited to a maximum of 30 m, to reduce timestep restrictions. The hydraulic roughness in the model was specified as a spatially varying field, both for the flow and the wave related friction. Therefore, a bed type classification was derived from the BIRNM benthic habitat data of Batista (2012), in which we retained 3 classes for which we differentiate bottom friction parameters f_w and Chézy values following Storlazzi et al. (2017): (a) sandy patches: $f_w = 0.1$ and Chézy= $55\,\mathrm{m}^{0.5}/\mathrm{s}$ (b) patch reef with <10% coral cover: $f_w = 0.15$ and Chézy= $30\,\mathrm{m}^{0.5}/\mathrm{s}$ (c) patch reef with <50% coral cover: $f_w = 0.3$ and Chézy= $20\,\mathrm{m}^{0.5}/\mathrm{s}$.

Offshore wave data were not available at the time of the field campaign, therefore a nested regional SWAN (Booij et al. (1999); version 41.31) wave model was constructed to derive wave boundary conditions for the surfbeat model. We included the effects of wind wave growth, refraction, depth-induced wave breaking (Battjes and Janssen, 1978), whitecapping (van der Westhuysen et al., 2007) and bottom friction ((Hasselmann et al., 1973)) with default parameters. The large SWAN domain covers the Atlantic north of the British Virgin Islands until the Caribbean Sea south of St.-Croix at a uniform resolution of 1500 m. The finer nested domain has a resolution of 200 m and covers the north coast of St.-Croix. The SWAN model was forced with ERA5 (Hersbach et al., 2020) wind and wave data, and validated against 5 months (Jun 1st–Oct 31th 2010) of buoy data at Christiansted (CDIP station 431, Fig. 18(a)). Significant wave heights were estimated with a bias of 0.0 m and a RMSE of 0.20 m, and the T_{m01} with a bias of 0.23 s and an RMSE of 1.24 s. The SWAN model was subsequently run for the period January 11–15 2016, and hourly wave parameters were extracted at the N side of the barrier reef to construct parametric JONSWAP time series to force the surfbeat model (Fig. 19(b–d)). The water level signal to force the N absorbing–generating model boundary was taken from station N1 as is (Fig. 19(a)), as comparison with a tidal harmonics fit showed considerable NTR influence uncorrelated with the incident wave climate. Local wind was insignificant during the model

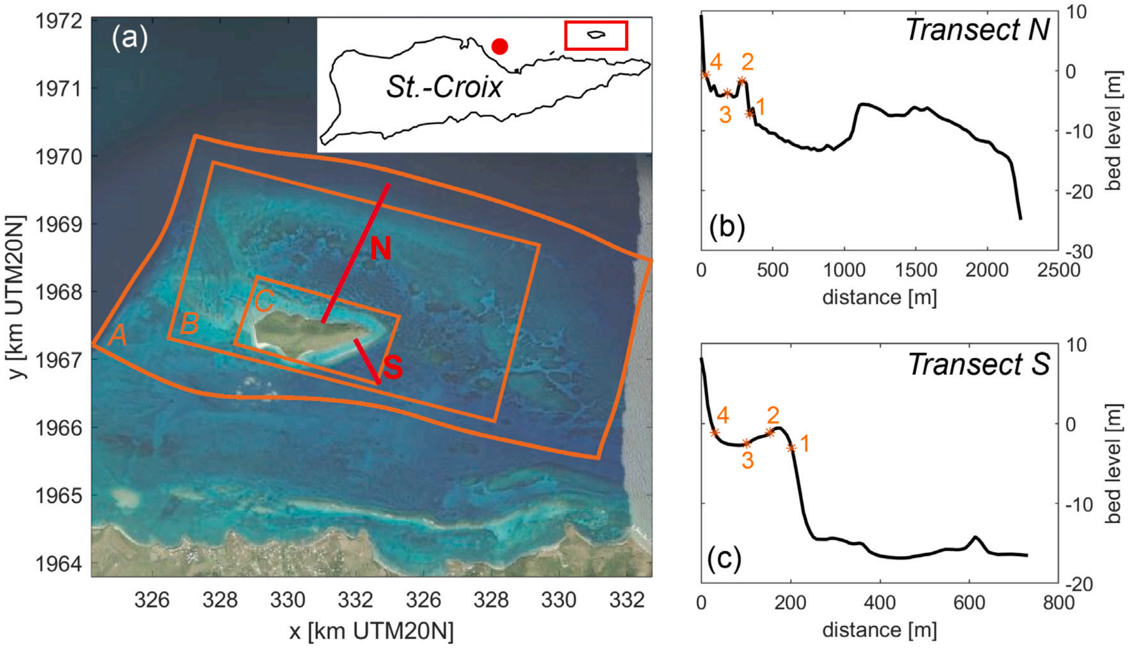

Fig. 18. Buck Island model setup. (**a**) Grid outline (A) and internal grid refinement areas (B,C). The respective grid resolutions are approximately 30.0 m, 15.0 m and 7.5 m. At the fringing reef locations, the grid is further refined to 3.0 m. Inset: Location of Buck Island off the NE coast of St.-Croix. Red dot indicates the location of the Christiansted CDIP wave buoy used for the regional wave model verification; (**b**) Bed level and instrument positions along transect N; (**c**) Bed level and instrument positions along transect S. Satellite imagery copyright Earthstar Geographics.

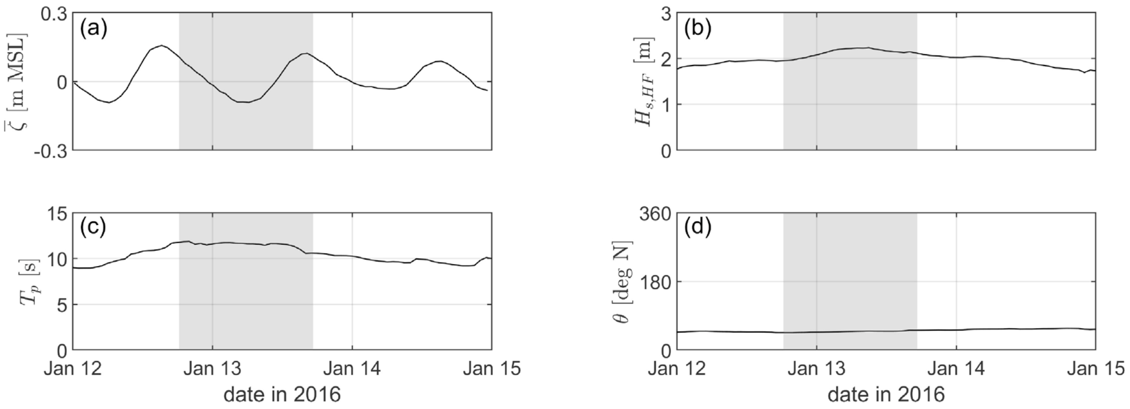

Fig. 19. Offshore boundary conditions Buck Island model. Grey bar indicates the model period. (**a**) Tide level derived from station N1 (Rosenberger et al., 2020a); (**b–d**) Wave data derived from regional SWAN model: (**b**) Offshore significant wave height; (**c**) peak wave period; (**c**) mean wave direction.

period (NOAA, 2022), and was not taken into account. The model was run on 20 partitions.

Modelled water levels and wave data were recorded continuously at 2 Hz in the locations of the 8 deployment sites. In order to obtain results that are compatible with the USGS dataset, hourly 2048 s bursts of the demeaned water levels ζ were bandpass-filtered to obtain the low-frequency signal ζ_{LF} (0.004 – 0.04 Hz) and the high frequency signal ζ_{HF} (0.04 – 0.4 Hz). The corresponding rms LF wave height was then obtained by $H_{rms,LF} = \sqrt{8\,\overline{\zeta^2_{LF}}}$, the rms short wave height $H_{rms,HF}$ as $\sqrt{H^2_{modelled} + 8\,\overline{\zeta^2_{HF}}}$.

3.6.2. Results

The mean water level variability in the observation stations is well reproduced in the model (Fig. 20(a–h)). The tide levels in stations N1 and S1 are simulated correctly, with small biases. The cross-reef distribution of the sea swell wave setup values over both transects is modelled correctly, as is the difference in setup magnitude between the *N* and the S transect. Sea–swell (SS) wave heights are modelled with an absolute bias and a RMSE of ~0.05 m. Significant amounts of SS wave energy (>50%) are dissipated over the barrier reef and the lagoon. Inspection of the spatial distribution of the SS wave dissipation fields from the model output suggests that this wave height reduction occurs mainly through bottom frictional effects (Fig. 20(i–p)). The resulting reef face wave heights in N1 are about twice as high as those in the more sheltered S1 station. Significant SS wave breaking only takes place around the crest of the fringing reef for the wave heights considered in this study. As a result, N1 and S1 SS wave heights are tide–independent, but HF wave heights on the reef flat and in the fringing reef lagoon (N2–4, S2–4) are largely determined by the local water depth over the reef crest. Modelled LF wave height error statistics are similar in magnitude as the HF ones, and errors are generally smaller than 20%, except for station S1 (Fig. 20(q–x)). Inspection of the spatial distribution of the water level variance in the model domain indicates two sources of local surfbeat generation. On the relatively gently sloping barrier reef, IG waves are generated as a result of SS wave energy dissipation through bottom friction, as wave breaking is generally absent. On the fringing reef face and reef crest, IG waves are generated through the breakpoint

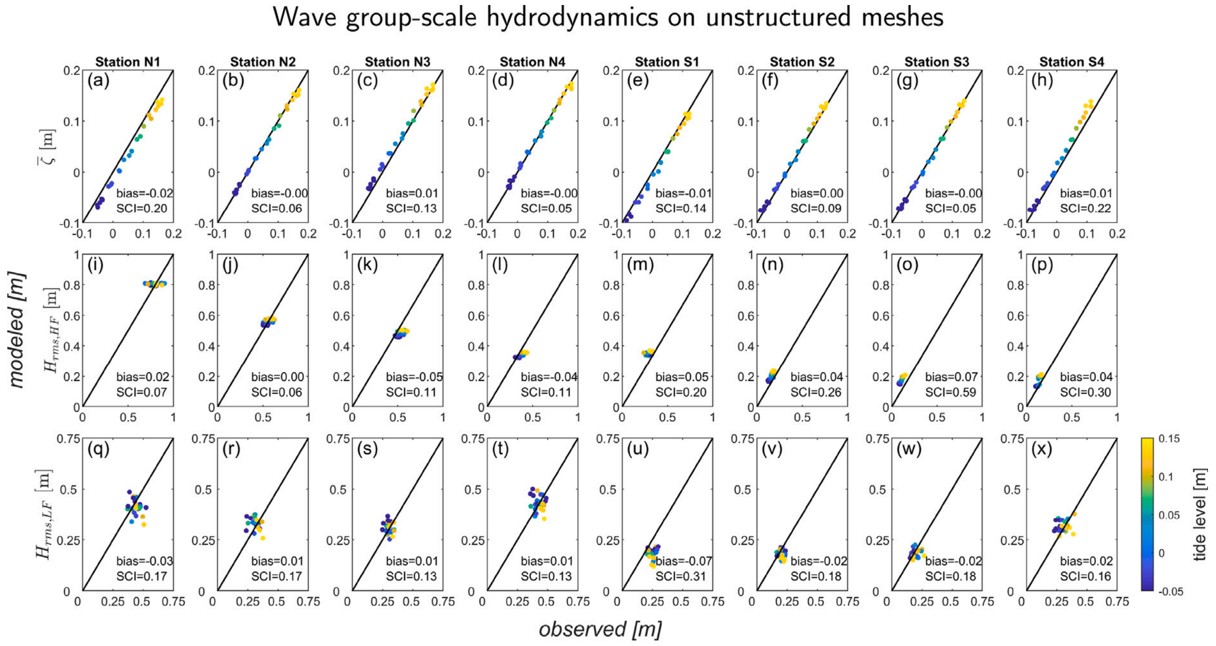

Fig. 20. Model–data comparison BIRNM: **(a–h)** mean water level $\bar{\zeta}$; **(i–p)** SS wave height $H_{rms,HF}$; **(q–x)** IG wave height $H_{rms,LF}$. Dots are coloured by the tide level imposed on the offshore boundary.

forcing mechanism (normalised bed slope parameter β_b (Battjes et al., 2004) equal to ~2). The model is able to reproduce the relative cross-reef spatial pattern in IG wave heights on both transects, including the higher IG values observed in the two stations closest to the shoreline, N4 an S4, which result from long wave reflection off the steep shoreline. Fig. 20(q–x) suggests a tidal dependence of the IG wave heights on transect *N* in the measured data. This was verified not to be the case from the complete measured time series in station N1.

In conclusion, this test case demonstrates that the model is able to reproduce the propagation and dissipation of sea swell wave fields, and the associated IG wave dynamics on larger spatial scales in a complex model domain, using boundary conditions generated from a global wave and wind database. As for efficiency, the average achieved timestep in this unstructured surfbeat run was 0.14 s for a CFL condition of 0.7. Comparison with a structured XBeach model setup for the same problem shows an improvement of the timestep with roughly 40% and a reduction in grid size by a factor of 2.9, while attaining a spatial resolution on the fringing reef that was 2 times better.

Table A.1
Wave breaking formulations.

Wave model type	Wave breaking formula	Reference
Stationary	Baldock Janssen&Battjes	Baldock et al. (1998) Janssen and Battjes (2007)
Nonstationary	Roelvink 1993 original Roelvink 1993 scaled Roelvink&Daly	Roelvink (1993a) Roelvink (1993a) Daly et al. (2012)

4. Summary and conclusions

This paper presents the first numerical model, defined on an unstructured mesh administration, that is able to resolve hydrodynamics forced by tides, wind, and sea–swell waves on the time scale of wave groups. We have validated different functionalities in a series of six tests, showing that the model has good skill in reproducing measured laboratory and field data, as well as results from semi-analytical model approaches.

The Zelt test case was included to verify the correct propagation of long waves, flooding and drying, and the robustness of the offshore flow boundary in absorbing reflected free waves leaving the model domain under highly oblique angles. Additionally, the implementation of the drying and wetting algorithm was compared favourably to results from a temporally and spatially adaptive grid modelling approach. Results proved to be robust under different grid configurations. The use of a triangular grid alleviated grid influences in the phasing of the run-up solution.

The Boers test demonstrated the model's capability of generating first- and second-order boundary forcing, the functioning of the 1D absorbing flow boundary, the correct implementation of dissipation by wave breaking, and of the wave forces in the momentum balance. The laboratory data were in general well reproduced, although the simulation of the steepest wave conditions proved more challenging, as we are using linear wave theory.

The DELILAH field case served as a verification for the stationary refraction (single direction) approach, which serves to counter the numerical diffusion of wave groups when advecting wave action in multiple directional bins over longer travel distances. Comparing the single direction, and the multiple directions results to data measured at the Duck Field Research Facility, the former method yields better results in reproducing the infragravity energy profile in the surf zone, and is better at retaining the wave group structure. The methods are on par in simulating the short wave distribution and the longshore current over the cross-shore profile. Combined with the possibility of localised refinement by using unstructured grids, the stationary refraction approach offers the possibility of significantly speeding up the calculations without loss of reliability.

The COAST3D field case reproduced the hydrodynamic response of a mildly sloping double barred sandy beach to a storm. Mean water depths and short wave heights were well reproduced during highly non-stationary conditions where incident wave heights and directions changed strongly over the course of a tide. Despite the fact that IG mean periods were correctly modelled, the IG wave height was underestimated due to the lack of a mechanism to let free IG enter through the domain boundaries.

The PILOT field case demonstrated the model's robustness in a challenging study area featuring longshore bathymetry variability with very steep gradients, a narrow surf zone and large bottom roughness.

Table B.1
Error metric definitions.

Parameter	Formula (m=measured; c=computed)	Description
Pearson correlation ρ	$Cov(m,c)/\sigma_m \sigma_c$	Correlation coefficient, indicating strength of a linear relationship between random variables m and c
Scatter Index SCI	$\frac{\sqrt{\overline{(c-m)^2}}}{\max(\sqrt{\overline{m^2}},\lvert\overline{m}\rvert)}$	Relative measure of the scatter between model and data. The error is normalised with the maximum of the rms of the data and the absolute value of the mean of the data; this avoids strange results for data with small mean and large variability
Relative bias	$\frac{\overline{c-m}}{\max(\sqrt{\overline{m^2}},\lvert\overline{m}\rvert)}$	This is a relative measure of the bias, normalised in the same way as the Scatter Index
Brier skill	$1.0-\frac{var(c-m)}{var(m)}$	This parameter relates the variance of the difference between data and model to the variance of the data. skill=1 means perfect skill; skill=0 means no skill; skill<0 means result is worse than doing nothing.

Using the parallel implementation of the model, the cross-shore and longshore variability of the short waves, the infragravity energy and the steady wave setup were skilfully resolved.

Finally, the Buck Island field case reproduced the propagation of an energetic swell field around an island protected by 2 reefs. On both the exposed measurement sites and the sheltered ones, bulk wave characteristics were correctly modelled starting from boundary conditions derived from a global reanalysis dataset, demonstrating the applicability of our approach in typical engineering studies.

The use of this unstructured wave model allows for coverage of the same model domain, with optimised resolution, yet with a smaller total number of grid cells. The model also allows a larger explicit average timestep for the same value of the CFL criterion, compared to structured models with similar functionality. The model reliably reproduces observations in laboratory and field conditions, and is as such widely deployable in a variety of simple and complex coastal settings to study nearshore hydrodynamics.

CRediT authorship contribution statement

Johan Reyns: Conceptualization, Software, Validation, Formal analysis, Writing – original draft. **Robert McCall:** Software. **Roshanka Ranasinghe:** Writing – review & editing. **Ap van Dongeren:** Writing – review & editing, Funding acquisition. **Dano Roelvink:** Conceptualization, Software, Writing – review & editing, Funding acquisition.

Declaration of competing interest

The authors declare that they have no known competing financial interests or personal relationships that could have appeared to influence the work reported in this paper.

Data availability

Data will be made available on request.

Acknowledgements

The authors would like to acknowledge Sander van der Pijl for his assistance in the development of the software. Janet Becker and Mark Merrifield provided the PILOT data, and are thanked for fruitful discussions on the Ipan reef dynamics. Bart Grasmeijer provided the COAST3D data and reports. Ellen Quataert substantially improved a first version of the BIRNM XBeach model. Permission to use data provided by the Field Research Facility of the U.S. Army Engineer Waterways Experiment Station's Coastal Engineering Research Center is appreciated.

Funding

This research was supported by The Pacific Community (SPC), New Caledonia under the WACOP project, by Deltares, The Netherlands under Strategic Research Programmes 'Natural Hazards' and 'Knowledge Foundation Software and Models', and by the Office of Naval Research, USA under award number N00014-17-1-2459. Work on the PILOT model benefited from two research visits to UH.

Appendix A. Overview of implemented formulations for wave energy dissipation by breaking

See Table A.1.

Appendix B. Performance metrics verification runs

B.1. *Error metrics*

See Table B.1.

B.2. *Boers flume tests*

See Table B.2.

B.3. *Zelt tsunami run-up*

See Table B.3.

B.4. *DELILAH field experiment*

See Table B.4.

B.5. *COAST3D Egmond campaign*

See Table B.5.

B.6. *PILOT field experiment*

See Table B.6.

Table B.2
Error statistics for the Boers (1996) flume study. S=spectral boundary conditions; M=measured boundary conditions. Note that the magnitude of the setup is $\mathcal{O}(0.001)$ m, so small deviations result in seemingly large error values.

Run	Parameter	ρ	SCI	Rel bias	Skill
S/1A	$setup$	0.93	1.18	1.09	−0.40
	$Hm0_{HF}$	0.98	0.04	−0.01	1.00
	$Hm0_{LF}$	0.50	0.14	−0.10	0.98
S/1B	$setup$	0.93	0.51	0.41	0.74
	$Hm0_{HF}$	0.98	0.04	−0.01	1.00
	$Hm0_{LF}$	0.70	0.10	−0.08	0.99
S/1C	$setup$	0.95	0.65	0.53	0.58
	$Hm0_{HF}$	0.98	0.07	−0.06	0.99
	$Hm0_{LF}$	0.72	0.15	0.12	0.98
M/1A	$setup$	0.93	0.98	0.84	0.04
	$Hm0_{HF}$	0.98	0.05	0.01	1.00
	$Hm0_{LF}$	0.69	0.10	−0.05	0.99
M/1B	$setup$	0.94	0.52	0.37	0.73
	$Hm0_{HF}$	0.98	0.07	0.04	1.00
	$Hm0_{LF}$	0.70	0.14	−0.12	0.98
M/1C	$setup$	0.94	0.34	−0.01	0.89
	$Hm0_{HF}$	0.98	0.05	−0.02	1.00
	$Hm0_{LF}$	0.74	0.10	−0.03	0.99

Table B.3
Error statistics for water level time series of the Zelt (1986) tsunami run-up case. R: rectangular grid; T: triangular grid; θ_g: grid rotation angle.

Run	ρ	SCI	Rel bias	Skill
(1) $R - \theta_g = 0°$	0.96	0.27	0.07	0.93
(2) $R - \theta_g = 30°$	0.98	0.20	0.07	0.96
(3) $T - \theta_g = 0°$	0.98	0.17	0.07	0.97

Table B.4
Error statistics for the DELILAH field case. SDir: Single direction run; MDir: Multiple direction run.

Run	Parameter	ρ	SCI	Rel bias	Skill
Sdir	$H_{rms,HF}$	0.78	0.12	−0.02	0.99
	$H_{rms,LF}$	0.70	0.07	−0.01	0.99
	v	0.76	0.28	0.18	0.92
Mdir	$H_{rms,HF}$	0.77	0.12	0.04	0.99
	$H_{rms,LF}$	0.60	0.10	0.00	0.99
	v	0.76	0.35	0.28	0.87

Table B.5
Error statistics for the COAST3D field case for October 25th 1998 09:00. Values are averaged over all observations stations.

Parameter	ρ	SCI	Rel bias	Skill
$depth$	0.85	0.07	0.05	0.99
$H_{rms,HF}$	0.84	0.05	−0.01	0.99
$H_{rms,LF}$	0.28	0.085	−0.06	0.99

Table B.6
Error statistics for the PILOT field case.

Parameter	ρ	SCI	Rel bias	Skill
$Hm0_{HF}$	0.79	0.10	0.02	0.99
$Hm0_{LF}$	0.70	0.17	0.06	0.97
$\bar{\zeta}$	0.85	0.063	−0.00	0.99

Appendix C. Implicit stationary wave energy solver

In order to determine the mean wave direction over the unstructured grid while taking into account refraction and dissipation, we solve the simplified wave energy balance Eq. (28) in wave direction θ:

$$\frac{\partial ee}{\partial t} + \frac{\partial c_g\, ee}{\partial s} + \frac{\partial c_\theta\, ee}{\partial \theta} + dd = 0 \tag{28}$$

where ee is the spectral wave energy density per node and wave direction, t is time, c_g is the group velocity, s is the distance along the wave direction under consideration, c_θ is the refraction velocity, θ is the wave direction, and dd is the local wave dissipation. Eq. (28) is discretised with finite differences at the location of the network nodes using a forward Euler scheme in time, and an implicit first order upwind approach in geographical and directional space. After rearranging the terms in the equation, this results in a tridiagonal coefficient matrix and a right hand side that is a function of the wave energy at the previous timestep ee^n_k, and the already updated wave energy at the upwind neighbours ee^{n+1}_{kupw}. This system can be solved with standard methods, such as the Thomas algorithm (Press et al., 2007).

On open wave boundaries a Dirichlet wave energy condition is applied, while on other open, non-wave boundaries, a zero gradient Neumann wave energy condition is imposed. The system of equations is solved consecutively along four orthogonal sweep directions, starting along the incident wave direction on the open model boundary. Local wave energy values are determined from (partially) converged upwind node values. By iterating the sweeping process and applying relaxation, we can solve for the effect of the non-linear dissipation term dd. A user defined criterion determines when the solution process has converged. After interpolation to the flow administration cell centres, the mean wave direction is determined from the directional distribution of the wave energy.

References

Anarde, K., Figlus, J., Sous, D., Tissier, M., 2020. Transformation of infragravity waves during hurricane overwash. J. Mar. Sci. Eng. 8, 545.

Andrews, D., McIntyre, M., 1978. An exact theory of nonlinear waves on a Lagrangian-mean flow. J. Fluid Mech. 89, 609–646.

Baldock, T., 2012. Dissipation of incident forced long waves in the surf zone–implications for the concept of "bound" wave release at short wave breaking. Coast. Eng. 60, 276–285. http://dx.doi.org/10.1016/j.coastaleng.2011.11.002.

Baldock, T., Holmes, P., Bunker, S., Van Weert, P., 1998. Cross-shore hydrodynamics within an unsaturated surf zone. Coast. Eng. 34, 173–196.

Batista, T., 2012. Benthic habitat mapping for Buck Island Reef National Monument, St. Croix. URL: https://maps.coastalscience.noaa.gov/biomapper/biomapper.html?id=BUIS.

Battjes, J., 1975. Modelling of turbulence in the surfzone. In: ASCE Symposium on Modelling Techniques. San Diego, California, ASCE, San Francisco, California.

Battjes, J.A., Bakkenes, H.J., Janssen, T.T., van Dongeren, A.R., 2004. Shoaling of subharmonic gravity waves. J. Geophys. Res. 109, http://dx.doi.org/10.1029/2003jc001863.

Battjes, J., Janssen, J., 1978. Energy loss and set-up due to breaking of random waves, 1, 32. http://dx.doi.org/10.9753/icce.v16.32.

Baumann, J., Chaumillon, E., Bertin, X., Schneider, J.L., Guillot, B., Schmutz, M., 2017. Importance of infragravity waves for the generation of washover deposits. Mar. Geol. 391, 20–35.

Bertin, X., Oliveira, A., Fortunato, A.B., 2009. Simulating morphodynamics with unstructured grids: Description and validation of a modeling system for coastal applications. Ocean Model. 28, 75–87.

Billson, O., Russell, P., Davidson, M., 2019. Storm waves at the shoreline: When and where are infragravity waves important? J. Mar. Sci. Eng. 7, 139.

Birkemeier, W.A., Donoghue, C., Long, C.E., Hathaway, K.K., Baron, C.F., 1997. 1990 DELILAH Nearshore Experiment: Summary Report. techreport CHL-97-24, US Army Engineer Waterways Experiment Station.

Boers, M., 1996. Simulation of a Surf Zone with a Barred Beach. Report 1. Wave heights and wave breaking. Communications on Hydraulic and Geotechnical Engineering 1996-05, TU Delft, URL: http://resolver.tudelft.nl/uuid:22dfbc0a-adf8-44cb-9659-9d0a366c88d6.

Booij, N., Ris, R.C., Holthuijsen, L.H., 1999. A third-generation wave model for coastal regions: 1, model description and validation. J. Geophys. Res.: Oceans 104, 7649–7666.

Bowen, A., Inman, D., Simmons, V., 1968. Wave 'set-down' and set-up. J. Geophys. Res. 73, 2569–2577.

CDIP, 2021. Coastal data information program. http://cdip.ucsd.edu/m/products/?stn=121p1.

Celik, I.B., Ghia, U., Roache, P.J., Freitas, C.J., Coleman, H., Raad, P.E., 2008. Procedure for estimation and reporting of uncertainty due to discretization in CFD applications. J. Fluids Eng. 130, 078001. http://dx.doi.org/10.1115/1.2960953.

Cheriton, O.M., Storlazzi, C.D., Rosenberger, K.J., 2016. Observations of wave transformation over a fringing coral reef and the importance of low-frequency waves and offshore water levels to runup, overwash, and coastal flooding. J. Geophys. Res.: Oceans 121, 3121–3140.

Cheriton, O.M., Storlazzi, C.D., Rosenberger, K.J., 2020. In situ observations of wave transformation and infragravity bore development across reef flats of varying geomorphology. Front. Mar. Sci. 7 (351), http://dx.doi.org/10.3389/fmars.2020.00351, URL: https://www.frontiersin.org/article/10.3389/fmars.2020.00351.

Cienfuegos, R., Duarte, L., Suarez, L., Catalán, P., 2010. Numerical computation of infragravity wave dynamics and velocity profiles using a fully nonlinear boussinesq model. In: Coastal Engineering Proceedings. ASCE, http://dx.doi.org/10.9753/icce.v32.currents.48.

Clark, S.J., Becker, J.M., Merrifield, M.A., Behrens, J., 2020. The influence of a crossreef channel on the wavedriven setup and circulation at IPAN, Guam. J. Geophys. Res.: Oceans 125, e2019JC015722.

Contardo, S., Lowe, R.J., Hansen, J.E., Rijnsdorp, D.P., Dufois, F., Symonds, G., 2021. Free and forced components of shoaling long waves in the absence of short-wave breaking. J. Phys. Oceanogr. 51, 1465–1487.

Contardo, S., Symonds, G., Dufois, F., 2018. Breakpoint forcing revisited: Phase between forcing and response. J. Geophys. Res.: Oceans 123, 1354–1363.

Courant, R., Friedrichs, K., Lewy, H., 1967. On the partial difference equations of mathematical physics. IBM J. Res. Dev. 11, 215–234.

Daly, C., Roelvink, D., van Dongeren, A., de Vries, J.v.T., McCall, R., 2012. Validation of an advective-deterministic approach to short wave breaking in a surf-beat model. Coast. Eng. 60, 69–83.

de Bakker, A., Brinkkemper, J., Van der Steen, F., Tissier, M., Ruessink, B., 2016a. Cross-shore sand transport by infragravity waves as a function of beach steepness. J. Geophys. Res.: Earth Surf. 121, 1786–1799.

de Bakker, A.T.M., Herbers, T.H.C., Smit, P.B., Tissier, M.F.S., Ruessink, B.G., 2015. Nonlinear infragravity–wave interactions on a gently sloping laboratory beach. J. Phys. Oceanogr. 45, 589–605. http://dx.doi.org/10.1175/jpo-d-14-0186.1.

de Bakker, A., Tissier, M., Ruessink, B., 2016b. Beach steepness effects on nonlinear infragravity-wave interactions: A numerical study. J. Geophys. Res.: Oceans 121, 554–570.

de Ridder, M.P., Smit, P.B., van Dongeren, A.R., McCall, R.T., Nederhoff, K., Reniers, A.J., 2021. Efficient two-layer non-hydrostatic wave model with accurate dispersive behaviour. Coast. Eng. 164, 103808.

Deltares, 2021. D-Flow Flexible Mesh, Technical Reference Manual. Technical Report, Deltares, URL: http://content.oss.deltares.nl/delft3d/manuals/D-Flow_FM_Technical_Reference_Manual.pdf.

Dietrich, J.C., Tanaka, S., Westerink, J.J., Dawson, C.N., Luettich, R., Zijlema, M., Holthuijsen, L.H., Smith, J., Westerink, L., Westerink, H., 2012. Performance of the unstructured-mesh, swan+ adcirc model in computing hurricane waves and surge. J. Sci. Comput. 52, 468–497.

Drost, E.J., Cuttler, M.V., Lowe, R.J., Hansen, J.E., 2019. Predicting the hydrodynamic response of a coastal reef-lagoon system to a tropical cyclone using phase-averaged and surfbeat-resolving wave models. Coast. Eng. 152, 103525.

Egbert, G.D., Erofeeva, S.Y., 2002. Efficient inverse modeling of barotropic ocean tides. J. Atmos. Ocean. Technol. 19, 183–204.

Elgar, S., Herbers, T.H.C., Okihiro, M., Oltman-Shay, J., Guza, R.T., 1992. Observations of infragravity waves. J. Geophys. Res. 97 (15573), http://dx.doi.org/10.1029/92jc01316.

Fiedler, J.W., Smit, P.B., Brodie, K.L., McNinch, J., Guza, R.T., 2018. Numerical modeling of wave runup on steep and mildly sloping natural beaches. Coast. Eng. 131, 106–113.

Fredericks, A.M., Kranenburg, C., Nagle, D.B., 2015. Eaarl-b submerged topography-saint croix, U.S. virgin islands. http://dx.doi.org/10.5066/F73T9F86, 2014. URL: http://coastal.er.usgs.gov/data-release/doi-F73T9F86/.

Guedes, R.M.C., Bryan, K.R., Coco, G., 2013. Observations of wave energy fluxes and swash motions on a low-sloping, dissipative beach. J. Geophys. Res.: Oceans 118, 3651–3669. http://dx.doi.org/10.1002/jgrc.20267.

Guérin, T., de Bakker, A., Bertin, X., 2019. On the bound wave phase lag. Fluids 4, URL: https://www.mdpi.com/2311-5521/4/3/152.

Guérin, X., Dodet, G., 2016. A numerical scheme for coastal morphodynamic modelling on unstructured grids. Ocean Model. 104, 45–53.

Guza, R., Thornton, E., 1985a. Velocity moments in nearshore. J. Waterw. Port Coast. Ocean Eng. 111, 235–256.

Guza, R.T., Thornton, E.B., 1985b. Observations of surf beat. J. Geophys. Res. 90 (3161), http://dx.doi.org/10.1029/jc090ic02p03161.

Hasselmann, K., 1962. On the non-linear energy transfer in a gravity-wave spectrum part 1, general theory. J. Fluid Mech. 12, 481–500.

Hasselmann, K., Barnett, T., Bouws, E., Carlson, H., Cartwright, D., Enke, K., Ewing, J., Gienapp, H., Hasselmann, D., Kruseman, P., Meerburg, A., Muller, P., Olbers, D., Richter, K., Sell, W., Walden, H., 1973. Measurements of wind-wave growth and swell decay during the joint north sea wave project (JONSWAP). Erganzungsheft Zur Deutschen Hydrografischen Zeitschrift Reihe A 8, 1–95.

Henderson, S.M., Guza, R.T., Elgar, S., Herbers, T.H.C., Bowen, A.J., 2006. Nonlinear generation and loss of infragravity wave energy. J. Geophys. Res. 111, http://dx.doi.org/10.1029/2006jc003539.

Herbers, T., Elgar, S., Guza, R., 1994. Infragravity-frequency (0.005–0.05 hz) motions on the shelf, Part I: Forced waves. J. Phys. Oceanogr. 24, 917–927.

Herbers, T.H.C., Elgar, S., Guza, R.T., 1995. Generation and propagation of infragravity waves. J. Geophys. Res. 100 (24863), http://dx.doi.org/10.1029/95jc02680.

Hersbach, H., Bell, B., Berrisford, P., Hirahara, S., Horányi, J., Nicolas, J., Peubey, C., Radu, R., Schepers, D., Simmons, A., Soci, C., Abdalla, S., Abellan, X., Balsamo, G., Bechtold, P., Biavati, G., Bidlot, J., Bonavita, M., Chiara, G.D., Dahlgren, P., Dee, D., Diamantakis, M., Dragani, R., Flemming, J., Forbes, R., Fuentes, M., Geer, A., Haimberger, L., Healy, S., Hogan, R.J., Hólm, E., Janisková, M., Keeley, S., Laloyaux, P., Lopez, P., Lupu, C., Radnoti, G., d. Rosnay, P., Rozum, I., Vamborg, F., Villaume, S., Thé paut, J.N., 2020. The ERA5 global reanalysis. Q. J. R. Meteorol. Soc. 146, 1999–2049.

Hirsch, C., 2007. Numerical Computation of Internal and External Flows, Volume 1: Fundamentals of Computational Fluid Dynamics, second ed. Butterworth-Heinemann.

Holman, R.A., Bowen, A.J., 1979. Edge waves on complex beach profiles. J. Geophys. Res. 84 (6339), http://dx.doi.org/10.1029/jc084ic10p06339.

Hou, J., Simons, F., Hinkelmann, R., 2012. Improved total variation diminishing schemes for advection simulation on arbitrary grids. Internat. J. Numer. Methods Fluids 70, 359–382.

Hubbard, M.E., Dodd, N., 2002. A 2D numerical model of wave run-up and overtopping. Coast. Eng. 47, 1–26. http://dx.doi.org/10.1016/s0378-3839(02)00094-7.

Janssen, T., Battjes, J., 2007. A note on wave energy dissipation over steep beaches. Coast. Eng. 54, 711–716.

Janssen, T.T., Battjes, J.A., van Dongeren, A.R., 2003. Long waves induced by short-wave groups over a sloping bottom. J. Geophys. Res. 108, http://dx.doi.org/10.1029/2002jc001515.

Karunarathna, H., Chadwick, A., Lawrence, J., 2005. Numerical experiments of swash oscillations on steep and gentle beaches. Coast. Eng. 52, 497–511.

Karunarathna, H., Tanimoto, K., 1995. Numerical experiments on low-frequency fluctuations on a submerged coastal reef. Coast. Eng. 26, 271–289.

Kernkamp, H.W., Van Dam, A., Stelling, G.S., de Goede, E.D., 2011. Efficient scheme for the shallow water equations on unstructured grids with application to the continental shelf. Ocean Dyn. 61, 1175–1188.

Klein, M.D., Elias, E.P.L., R, W.D.J, van Rijn, L.C., 2001. COAST3D - The Egmond Model: Hydrodynamic Validation of Delft3D with Field Measurements of Egmond-Main Field Experiment, October-November 1998. Technical Report Z2394, TU Delft and WL|Delft Hydraulics.

Kostense, J.K., 1985. Measurements of surf beat and set-down beneath wave groups. In: Coastal Engineering 1984. American Society of Civil Engineers, http://dx.doi.org/10.1061/9780872624382.050.

Lashley, C.H., Bertin, X., Roelvink, D., Arnaud, G., 2019. Contribution of infragravity waves to run-up and overwash in the pertuis breton embayment (France). J. Mar. Sci. Eng. 7, 205.

Lashley, C.H., Roelvink, D., van Dongeren, M.L., Lowe, R.J., 2018. Nonhydrostatic and surfbeat model predictions of extreme wave run-up in fringing reef environments. Coast. Eng. 137, 11–27. http://dx.doi.org/10.1016/j.coastaleng.2018.03.007.

Liao, Z., Li, S., Liu, Y., Zou, Q., 2021. An analytical spectral model for infragravity waves over topography in intermediate and shallow water under nonbreaking conditions. J. Phys. Oceanogr. 51, 2749–2765.

Liao, Z., Li, S., Paniagua-Arroyave, J.F., Liu, Y., Zou, Q., 2022. Infragravity wave amplification by isolated topography: Field observations and semi-analytical modeling. Appl. Ocean Res. 122, 103119. http://dx.doi.org/10.1016/j.apor.2022.103119.

List, J.H., 1991. Wave groupiness variations in the nearshore. Coast. Eng. 15, 475–496.

List, J.H., 1992. A model for the generation of two-dimensional surf beat. J. Geophys. Res.: Oceans 97, 5623–5635.

Longuet-Higgins, M.S., Stewart, R., 1962. Radiation stress and mass transport in gravity waves, with application to ‘surf beats’. J. Fluid Mech. 13, 481–504.

Longuet-Higgins, M.S., Stewart, R., 1964. Radiation stresses in water waves; A physical discussion, with applications. Deep-Sea Res. 11, 529–562.

Love, M.R., Sutherland, M., Beasley, L., Carignan, K.S., Eakins, B.W., 2015. Digital Elevation Models of the U.S. Virgin Islands: Procedures, Data Sources and Analysis. Technical Report, NOAA National Geophysical Data Center, Boulder, Colorado, URL: https://www.ngdc.noaa.gov/mgg/dat/dems/regional_tr/st_croix_13_mhw_2014.pdf.

Ma, G., Shi, F., Kirby, J.T., 2012. Shock-capturing non-hydrostatic model for fully dispersive surface wave processes. Ocean Model. 43, 22–35.

MacMahan, J.H., Reniers, A.J., Thornton, E.B., Stanton, T.P., 2004. Infragravity rip current pulsations. J. Geophys. Res.: Oceans 109.

Madsen, P.A., Sørensen, H., 1997. Surf zone dynamics simulated by a boussinesq type model, Part II: Surf beat and swash oscillations for wave groups and irregular waves. Coast. Eng. 32, 289–319.

Martyr-Koller, R., Kernkamp, H., Van Dam, A., Wegen, M.van der., Lucas, L., Knowles, N., Jaffe, B., Fregoso, T., 2017. Application of an unstructured 3D finite volume numerical model to flows and salinity dynamics in the San Francisco Bay-Delta. Estuar. Coast. Shelf Sci. 192, 86–107.

Massel, S.R., 1989. Hydrodynamics of Coastal Zones. Elsevier.

Masselink, G., 1995. Group bound long waves as a source of infragravity energy in the surf zone. Cont. Shelf Res. 15, 1525–1547. http://dx.doi.org/10.1016/0278-4343(95)00037-2.

McCall, R.T., De Vries, J.V.T., Plant, N., Van Dongeren, A., Roelvink, J., Thompson, D., Reniers, A., 2010. Two-dimensional time dependent hurricane overwash and erosion modeling at Santa Rosa Island. Coast. Eng. 57, 668–683.

Moura, T., Baldock, T.E., 2019. The influence of free long wave generation on the shoaling of forced infragravity waves. J. Mar. Sci. Eng. 7 (305), http://dx.doi.org/10.3390/jmse7090305.

Nadaoka, K., Kondoh, T., 1982. Laboratory measurements of velocity field structure in the surf zone by LDV. Coast. Eng. Japan 25, 125–145.

Nairn, R.B., Roelvink, J., Southgate, H.N., 1991. Transition zone width and implications for modelling surfzone hydrodynamics. In: Coastal Engineering 1990. pp. 68–81.

NCCOS, 2004. Benthic habitats of Guam derived from IKONOS imagery, 2001–2003. http://coastalscience.noaa.gov/datasets/ccma/biogeo/us_pac_terr/habitats/guam_habitat.zip.

Nguyen, D.T., Jacobsen, N.G., Roelvink, D., 2021. Development and validation of Quasi-Eulerian mean three-dimensional equations of motion using the generalized Lagrangian mean method. J. Mar. Sci. Eng. 9 (76).

NOAA, 2008. Guam 1/3 arc-second MHW coastal digital elevation model. https://www.ncei.noaa.gov/metadata/geoportal/rest/metadata/item/gov.noaa.ngdc.mgg.dem:586/html.

NOAA, 2018. 2007 Joint airborne LiDAR bathymetry technical center of expertise (JALBTCX) topobathy LiDAR: Guam. https://coast.noaa.gov/htdata/lidar1_z/msl/data/551.

NOAA, 2020. Co-Ops tides and currents. https://tidesandcurrents.noaa.gov/products.html. (Accessed 30 September 2020).

NOAA, 2022. Christiansted Harbor, St Croix, VI - Station ID: 9751364. URL: https://tidesandcurrents.noaa.gov/stationhome.html?id=9751364.

Nwogu, O., Demirbilek, Z., 2010. Infragravity wave motions and runup over shallow fringing reefs. J. Waterw. Port Coast. Ocean Eng. 136, 295–305.

Okihiro, M., Guza, R., Seymour, R., 1992. Bound infragravity waves. J. Geophys. Res.: Oceans 97, 11453–11469.

Özkan-Haller, H.T., Kirby, J.T., 1997. A Fourier-Chebyshev collocation method for the shallow water equations including shoreline runup. Appl. Ocean Res. 19, 21–34.

Péquignet, A.C.N., Becker, J.M., Merrifield, M.A., 2014. Energy transfer between wind waves and low-frequency oscillations on a fringing reef, IPAN, Guam. J. Geophys. Res.: Oceans 119, 6709–6724. http://dx.doi.org/10.1002/2014JC010179.

Péquignet, A.C.N., Becker, J.M., Merrifield, M.A., Aucan, J., 2009. Forcing of resonant modes on a fringing reef during tropical storm Man-Yi. Geophys. Res. Lett. 36, http://dx.doi.org/10.1029/2008GL036259.

Perot, B., 2000. Conservation properties of unstructured staggered mesh schemes. J. Comput. Phys. 159, 58–89.

Pomeroy, A., Lowe, R., Symonds, G., Va. Dongeren, A., Moore, C., 2012. The dynamics of infragravity wave transformation over a fringing reef. J. Geophys. Res.: Oceans 117.

Press, W.H., Teukolsky, S.A., Vetterling, W.T., Flannery, B.P., 2007. Numerical Recipes: The Art of Scientific Computing, third ed. Cambridge University Press, New York, USA.

Reniers, A.J., MacMahan, J., Thornton, E.B., Stanton, T.P., 2006. Modelling infragravity motions on a rip-channel beach. Coast. Eng. 53, 209–222.

Reniers, A.J., MacMahan, J., Thornton, E., Stanton, T.P., Henriquez, M., Brown, J., Brown, J., Gallagher, E., 2009. Surf zone surface retention on a rip-channeled beach. J. Geophys. Res.: Oceans 114.

Reniers, A.J., Roelvink, J., Thornton, E., 2004. Morphodynamic modeling of an embayed beach under wave group forcing. J. Geophys. Res.: Oceans 109.

Reniers, A., Va. Dongeren, A., Battjes, J., Thornton, E., 2002. Linear modeling of infragravity waves during Delilah. J. Geophys. Res.: Oceans 107, 1.

Rijnsdorp, D.P., Buckley, M.L., d. Silva, R.F., Cuttler, M.V.W., Hansen, J.E., Lowe, R.J., Green, R.H., Storlazzi, C.D., 2021. A numerical study of wave-driven mean flows and setup dynamics at a coral reef-lagoon system. J. Geophys. Res.: Oceans 126, e2020JC016811. http://dx.doi.org/10.1029/2020JC016811, URL: https://agupubs.onlinelibrary.wiley.com/doi/abs/10.1029/2020JC016811, e2020JC016811 2020JC016811.

Rijnsdorp, D.P., Ruessink, G., Zijlema, M., 2015. Infragravity-wave dynamics in a barred coastal region, a numerical study. J. Geophys. Res.: Oceans 120, 4068–4089.

Risandi, J., Rijnsdorp, D.P., Hansen, J.E., Lowe, R.J., 2020. Hydrodynamic modeling of a reef-fringed pocket beach using a phase-resolved non-hydrostatic model. J. Mar. Sci. Eng. 8, http://dx.doi.org/10.3390/jmse8110877, URL: https://www.mdpi.com/2077-1312/8/11/877.

Roelvink, J., 1993a. Dissipation in random wave groups incident on a beach. Coast. Eng. 19, 127–150.

Roelvink, J., 1993b. Surf Beat and Its Effect on Cross-Shore profiles (Ph.D. thesis). Delft University of Technology.

Roelvink, D., Den Heijer, C., Van Thiel De Vries, J., 2013. Morphological modelling of strongly curved Islands. In: Coastal Dynamics 2013: 7th International Conference on Coastal Dynamics, Arcachon, France, 24-28 June 2013. Bordeaux University.

Roelvink, D., McCall, R., Mehvar, S., Nederhoff, K., Dastgheib, A., 2018. Improving predictions of swash dynamics in XBeach: The role of groupiness and incident-band runup. Coast. Eng. 134, 103–123.

Roelvink, D., Reniers, A., Van Dongeren, A., De Vries, J.V.T., McCall, R., Lescinski, J., 2009. Modelling storm impacts on beaches, dunes and barrier Islands. Coast. Eng. 56, 1133–1152.

Roelvink, D., Stelling, G., Hoonhout, B., Risandi, J., Jacobs, W., Merli, D., 2012. Development and field validation of a 2DH curvilinear storm impact model. In: ICCE 2012: Proceedings of the 33rd International Conference on Coastal Engineering, Santander, Spain, 1-6 July 2012. Coastal Engineering Research Council.

Roelvink, J., Stive, M., 1989. Bar-generating cross-shore flow mechanisms on a beach. J. Geophys. Res.: Oceans 94, 4785–4800.

Roelvink, J., Walstra, D.J., 2004. Keeping it simple by using complex models. Adv. Hydro-Sci. Eng. 6, 1–11.

Rosenberger, K.J., Cheriton, O.M., Storlazzi, C.D., 2020a. Cross-Reef Wave and Water Level Data from Coral Reef Environments (Ver. 2.0, March 2021). Geological Survey data release, U.S, http://dx.doi.org/10.5066/P9RYN5NH.

Rosenberger, K.J., Storlazzi, C.D., Cheriton, O.M., Pomeroy, A.W., Hansen, J.E., Lowe, R.J., Buckley, M.L., 2020b. Spectral wave-driven bedload transport across a coral reef flat/lagoon complex. Front. Mar. Sci. 7, 513020.

Ruessink, G., 1999. COAST 3D: Data Report 2.5D Experiment Egmond Aan Zee. Technical Report EC MAST Project No. MAS3-CT97-0086, IMAU, Utrecht University.

Ruessink, B.G., Miles, J.R., Feddersen, F., Guza, R.T., Elgar, S., 2001. Modeling the alongshore current on barred beaches. J. Geophys. Res.: Oceans 106, 22451–22463. http://dx.doi.org/10.1029/2000jc000766.

Sánchez-Arcilla A. Roelvink, J., O'Connor, B., Reniers, A., Jimenez, J., 1994. The delta flume'93 experiment. In: Proceedings Coastal Dynamics. pp. 488–502.

Sénéchal N. Dupuis, H., Bonneton, P., Howa, H., Pedreros, R., 2001. Observation of irregular wave transformation in the surf zone over a gently sloping sandy beach on the french atlantic coastline. Oceanol. Acta 24, 545–556. http://dx.doi.org/10.1016/s0399-1784(01)01171-9.

Shi, F., Svendsen, I.A., Kirby, J.T., Smith, J.M., 2003. A curvilinear version of a quasi-3D nearshore circulation model. Coast. Eng. 49, 99–124.

Soulsby, R., 1997. Dynamics of Marine Sands. Thomas Telford London.

Soulsby, R.L., 2001. Sediment transport and morphodynamics on complex coastlines–The coast3D project. In: Coastal Dynamics' 01. pp. 92–101,.

Storlazzi, C., Reguero, B., Lowe, E., Shope, J., Gibbs, A., Beck, M., Nickel, B., 2017. Rigorously valuing the role of coral reefs in coastal protection: An example from Maui, Hawaii, USA. In: Coastal Dynamics, Helsingor, Denmark. pp. 665–674.

Su, S.F., Ma, G., Hsu, T.W., 2015. Boussinesq modeling of spatial variability of infragravity waves on fringing reefs. Ocean Eng. 101, 78–92.

Symonds, G., Huntley, D.A., Bowen, A.J., 1982. Two-dimensional surf beat: Long wave generation by a time-varying breakpoint. J. Geophys. Res.: Oceans 87, 492–498.

Thanh, V.Q., Roelvink, D., Van Der Wegen, M., Tu, L.X., Reyns, J., Linh, V.T.P., 2020. Spatial topographic interpolation for meandering channels. J. Waterw. Port Coast. Ocean Eng. 146, 04020024.

Thompson, R.O., 1983. Low-pass filters to suppress inertial and tidal frequencies. J. Phys. Oceanogr. 13, 1077–1083.

Thomson, J., Elgar, S., Raubenheimer, B., Herbers, T.H.C., Guza, R.T., 2006. Tidal modulation of infragravity waves via nonlinear energy losses in the surfzone. Geophys. Res. Lett. 33, http://dx.doi.org/10.1029/2005gl025514.

Tissier, M., Bonneton, P., Michallet, H., Ruessink, B.G., 2015. Infragravity-wave modulation of short-wave celerity in the surf zone. J. Geophys. Res.: Oceans 120, 6799–6814. http://dx.doi.org/10.1002/2015jc010708.

van der Westhuysen, A.J., Zijlema, M., Battjes, J.A., 2007. Nonlinear saturation-based whitecapping dissipation in SWAN for deep and shallow water. Coast. Eng. 54, 151–170.

van Dongeren, A., Battjes, J., Janssen, T., van Noorloos, J., Steenhauer, K., Steenbergen, G., Reniers, A., 2007. Shoaling and shoreline dissipation of low-frequency waves. J. Geophys. Res. 112, http://dx.doi.org/10.1029/2006jc003701.

van Dongeren, A., Lowe, R., Pomeroy, A., Trang, D.M., Roelvink, D., Symonds, G., Ranasinghe, R., 2013. Numerical modeling of low-frequency wave dynamics over a fringing coral reef. Coast. Eng. 73, 178–190.

van Dongeren, A., Reniers, A., Battjes, J., Svendsen, I., 2003. Numerical modeling of infragravity wave response during DELILAH. J. Geophys. Res.: Oceans 108, http://dx.doi.org/10.1029/2002JC001332.

van Dongeren, A., Svendsen, I., 1997. Absorbing-generating boundary condition for shallow water models. J. Waterw. Port Coast. Ocean Eng. 123, 303–313.

Van Leeuwen, P.J., 1992. Low-Frequency Wave Generation Due to Breaking Wind Waves (Ph.D. thesis). Delft University of Technology.

van Rijn, L., Grasmeijer, B., Ruessink, G., 2000. COAST3D: Measurement Errors of Instruments for Velocity, Wave Height, Sand Concentration and Bed Levels in Field Conditions. Technical Report, Utrecht University and WL|Delft Hydraulics, URL: https://puc.overheid.nl/rijkswaterstaat/doc/PUC_117265_31/.

Vermetten, A., Schimmel, H., van Rijn, L., 2001. COAST3D Database Egmond Main Experiment October-November 1998. Technical Report Z2394.10, WL|Delft Hydraulics.

Vetter, O., Becker, J.M., Merrifield, M.A., Pequignet, A.C., Aucan, J., Boc, S.J., Pollock, C.E., 2010. Wave setup over a pacific island fringing reef. J. Geophys. Res.: Oceans 115, http://dx.doi.org/10.1029/2010JC006455.

Villaret, C., Hervouet, J.M., Kopmann, R., Merkel, U., Davies, A.G., 2013. Morphodynamic modeling using the Telemac finite-element system. Comput. Geosci. 53, 105–113.

Weir, B., Uchiyama, Y., Lane, E.M., Restrepo, J.M., McWilliams, J.C., 2011. A vortex force analysis of the interaction of rip currents and surface gravity waves. J. Geophys. Res. 116, http://dx.doi.org/10.1029/2010jc006232.

Wu, L., Chen, C., Guo, P., Shi, M., Qi, J., Ge, J., 2011. A FVCOM-based unstructured grid wave, current, sediment transport model, I. Model description and validation. J. Ocean Univ. China 10, 1–8.

Zelt, J.A., 1986. Tsunamis: The Response of Harbours with Sloping Boundaries to Long Wave Excitation (Ph.D. thesis). California Institute of Technology.

Zhang, Q., Toorman, E.A., Monbaliu, J., 2020. Shoaling of bound infragravity waves on plane slopes for bichromatic wave conditions. Coast. Eng. 158, 103684. http://dx.doi.org/10.1016/j.coastaleng.2020.103684, URL: https://www.sciencedirect.com/science/article/pii/S037838391930198X.

Zheng, P., Li, M., Zanden, J.van der., Wolf, J., Chen, X., Wang, C., et al., 2017. A 3D unstructured grid nearshore hydrodynamic model based on the vortex force formalism. Ocean Model. 116, 48–69.

Zijlema, M., Stelling, G., Smit, P., 2011. Swash: An operational public domain code for simulating wave fields and rapidly varied flows in coastal waters. Coast. Eng. 58, 992–1012.

Zou, Q., 2011. Generation, transformation, and scattering of long waves induced by a short-wave group over finite topography. J. Phys. Oceanogr. 41, 1842–1859.